energy&fuels

pubs.acs.org/EF

Article

Role of Organic Matter, Mineral, and Rock Fabric in the Full-Scale Pore and Fracture Network Development in the Mixed Lacustrine Source Rock System

Guangqing Yang, Jianhui Zeng,* Juncheng Qiao,* Yazhou Liu, Shengnan Liu, Wanting Jia, Weifu Cao, Chengyun Wang, Feng Geng, and Wenfei Wei

Cite This: *Energy Fuels* 2022, 36, 8161−8179

Read Online

ACCESS | Metrics & More | Article Recommendations

ABSTRACT: The mixed deposition constitutes the external clastic, intrabasinal, and pyroclastic components in both marine and lacustrine environments. The fine-grained mixed lacustrine source rocks are rich in organic matter and present good unconventional energy resources. However, the mixed lacustrine source rock systems have extremely low permeabilities and need hydraulic fracturing to stimulate oil from the complex nanoscale matrix. The role of rock fabric, organic matter, and mineral compositions in full-scale pore structures is still unclear, especially for the source rock from a mixed sedimentary environment. This restricts sweet spot identification. Here, we use three groups of Permian Lucaogou source rock samples with fine laminated, thick laminated, and massive rock fabric to investigate the relationship between rock fabric, organic matter, and pore structure using a combination of mineralogy, organic geochemistry, low-pressure nitrogen adsorption, micro-CT, and mercury injection capillary pressure data. The results indicate that the Lucaogou source rocks mainly contain type I and type II kerogen and show good to excellent hydrocarbon generation potential. The source rock was deposited in a mixed environment with high contents of carbonate and less siliceous minerals, showing good frackability. The mineralogy-based ternary classification shows that the source rock mainly belongs to high total organic carbon (TOC > 4%) mixed carbonate mudstone and high TOC mixed mudstone. For mixed lacustrine source rock, the full-scale pore-fracture distribution shows that the average percentage values of pore volume for micropores (<10 nm), transitional pores (10−100 nm), mesopores (100−1000 nm), and macropores (fracture) (>1000 nm) are 11.14, 21.62, 10.77, and 56.47%, respectively. However, the average percentage values of pore surface area for the abovementioned pores are 62.45, 30.45, 5.47, and 1.63%, respectively. Both quartz and terrigenous clast present a weak-medium unimodal correlation with the TOC content. Both terrigenous clast and clay minerals control the source rock hydrocarbon generation potential. The carbonate and terrigenous clast mineral content play a significant role in micropores and transitional pores, while the clay mineral presents a negative impact on macropore development. The effect of rock fabric on shale oil potential is negligible compared with organic matter abundance. Shales with thick parallel laminae and medium TOC (2% < TOC < 4%) possess favorable shale oil potential.

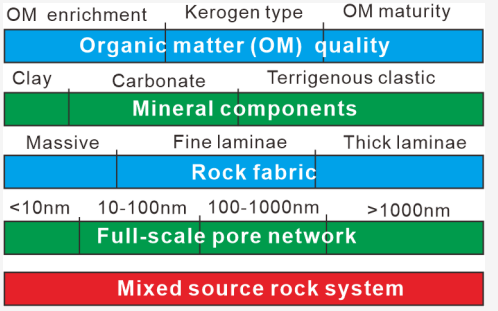

1. INTRODUCTION

Increasing energy demands make fine-grained sedimentary rocks become the active research field of petroleum exploration.[1−5] Specifically, the uptick in crude oil production in North America is mostly from shale oil. However, due to extremely low permeabilities and the need for hydraulic fracturing to stimulate oil from nanoscale shale matrixes,[6,7] the current shale oil recovery rate is less than 10%.[8−12] The current low oil recovery rate is strongly affected by shale pore structures and components including organic matter (OM) and minerals.[11]

The total organic carbon (TOC), mineral components, and maturity stage of shale affect the pore structure parameters and hydrocarbon primary migration.[13−16] A productive shale system should contain sufficient organic matter to support a percolating network, and this organic matter should be mature to build a pore system that percolates over a sufficiently large length scale.[17] Apart from the above parameters, lamina development is a widespread phenomenon in natural sedimentary rock.[18−20] The effect of laminae development is significant on the pore structure and intrasource migration of lacustrine shale.[21−24] Li et al.[21] presented that microfracture occurrence was at the boundary of laminae, and laminated shale had a better

Received: May 9, 2022
Revised: July 11, 2022
Published: July 22, 2022

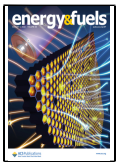

https://doi.org/10.1021/acs.energyfuels.2c01484
Energy Fuels 2022, 36, 8161−8179

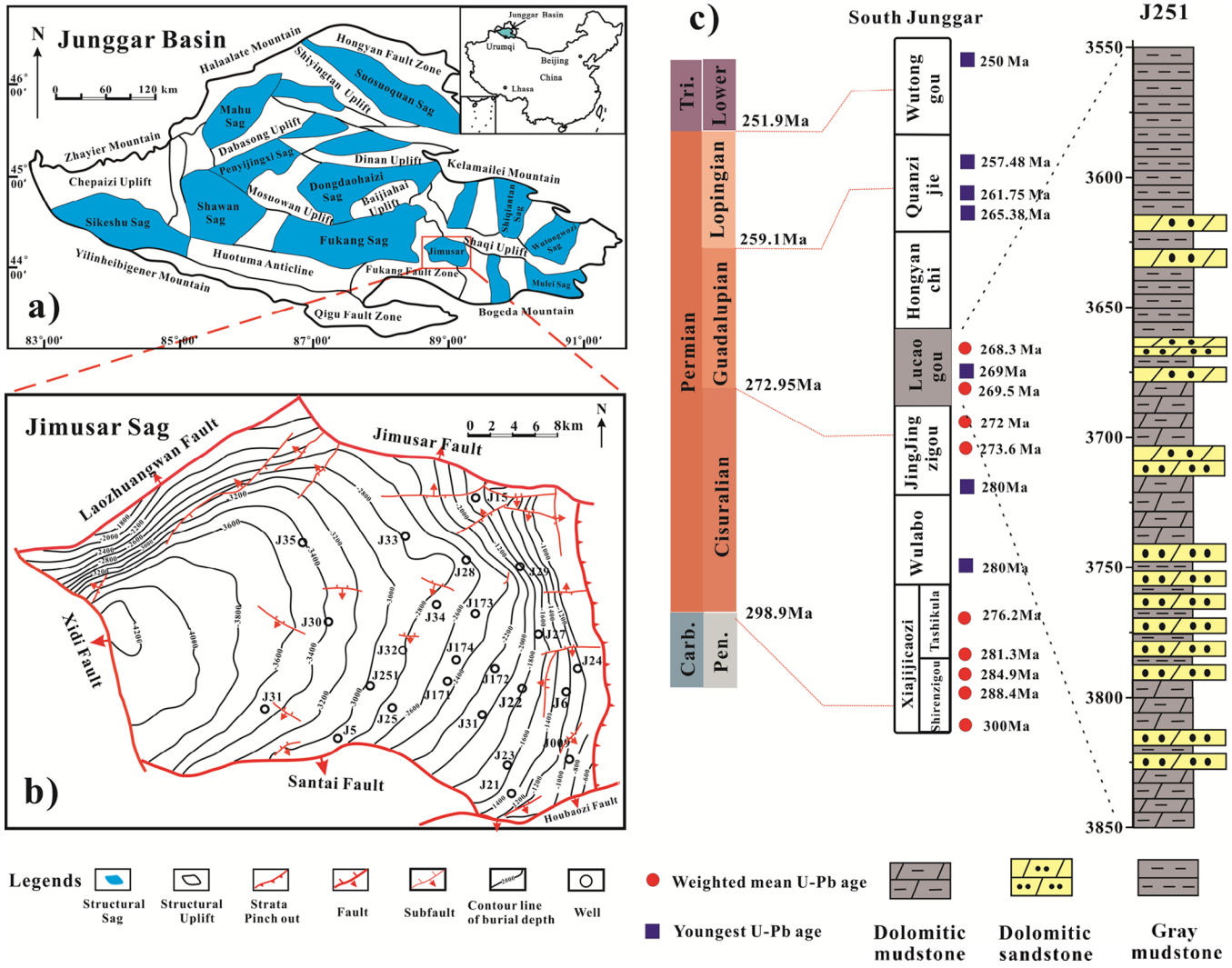

Figure 1. (a) Geological location of the Junggar Basin and detailed geological units in the Junggar Basin (modified from Cao et al.[47]) (b) Location of the wells of samples from Jimusar Sag (modified from Cao et al.[47]). (c) Generalized stratigraphic units in Jimusar Sag (modified from Huang et al.[48]).

connectivity than massive Shahejie mudstone in Zhanhua Sag, Eastern China. Lei et al.[25] analyzed the difference between silty laminae and clay laminae of Zhangjiatan Shale in the Ordos Basin. Their results showed that silty laminae had fewer micropores than adjacent clayed laminae, and the silty laminae play a role as a primary migration conduit. The solvent flow-through extraction experiment on shale from Eocene Shahejie Formation indicated that well-developed laminae could provide horizontal fracturing along the laminae boundary.[26] Furthermore, Liang et al.[27] analyzed the diagenetic fluid transport in Eocene lacustrine shale from Niuzhuang Sag, Bohai Bay Basin at the laminae scale. They concluded that varied laminae combinations are the key factors driving the distinct diagenetic characters. Specifically, laminated calcareous shale is strongly influenced by calcite recrystallization in the laminae boundary between calcite laminae and organic matter laminae.

The connectivity and morphological characters of pores in shale can be detected directly by micro-CT scanning[16] and fluid invasion methods including low-temperature N_2 adsorption[14,28,29] and mercury intrusion capillary pressure (MICP).[28] These analysis methods are widely utilized to analyze the pore volume (PV), the pore size distribution (PSD), and the specific surface area (SSA) quantitatively.[14,30−38] Apart from the classic pore division scheme recommended by the International Union of Pure and Applied Chemistry (IUPAC), the classification method by Hodot on pore structures for shale is applied as well.[36,37] Considering the scope of each method, in this study, we follow the Hodot coal pore classification, and pores in the source rock samples are divided into micropores (<10 nm), transitional pores (10−100 nm), mesopores (100−1000 nm), and macropores (>1000 nm).[32]

Generally, the sweet spot interval is mainly oil-bearing and presents greater values of porosity and permeability.[30] Under the current technical level, the oil production from the sweet spot section is economical.[31] In recent decades, the organic-rich laminated source rocks become a specific geologic sweet spot for shale oil resources.[38,39] Detailed research of the shale pore network development under varied rock fabrics is necessary for shale oil resource potential evaluation.[14,25] The Permian Lucaogou Formation (P_2l) in the Jimusar Sag, Junggar Basin is one of the hoariest world-class hydrocarbon-bearing shale intervals.[40,41] Interestingly, it is mixed with siliciclastic, carbonate, and tuffaceous deposits in the saline lake environment.[42] The unique multisource mixed sedimentary of the Lucaogou Formation makes the source rocks heterogeneous in both compositions and structures.[38] Shale oil exploration in this

https://doi.org/10.1021/acs.energyfuels.2c01484
Energy Fuels 2022, 36, 8161−8179

Table 1. TOC, R_o, Depth, and Maturity of Lucaogou Source Rock Samples

sample	R_o (%)	depth (m)	TOC (wt %)	S_1 (mg/g)	S_2 (mg/g)	T_{max} (°C)	HI (mg HC/g TOC)
24-18-FL	0.82	1691.40	1.06	1.01	5.77	435	545.37
22-8-FL	0.58	2541.40	5.27	3.22	31.26	446	592.83
43-12-FL	0.76	2950.50	5.99	2.61	37.18	443	620.39
305-9-FL	0.71	3405.86	4.57	4.49	25.51	438	558.21
32-6-FL	0.90	3577.40	10.58	2.32	54.15	437	511.81
23-10-TL	0.70	2295.50	6.12	2.82	35.93	443	587.48
301-2-TL	0.70	2751.93	2.14	2.47	10.75	439	501.87
31-14-TL	0.70	2859.20	2.61	11.99	16.88	434	647.24
43-1-TL	0.61	2953.00	11.44	3.20	58.61	439	512.33
303-9-MS	0.84	2577.80	1.66	1.53	6.18	442	373.41
27-8-MS	0.70	2298.40	2.50	1.97	14.93	446	598.16
301-9-MS	0.90	2756.10	4.57	1.20	21.76	445	475.94
37-5-MS	0.71	2853.90	7.58	2.20	40.04	445	528.02
176-6-MS	0.80	3171.70	7.78	4.06	32.79	442	421.36

type of interval is still a big challenge. Three kinds of sedimentary structures are interpreted from decreasing laminae thickness, i.e., thick laminated (TL), fine laminated (FL), and massive (MS).[43] The interbedded mudstone, siltstone, carbonate, and some tuffaceous laminae were widely distributed in Permian Lucaogou Formation.[38] The accumulation morphology of organic matter in laminated Lucaogou source rock is mainly along the laminae; however, these organic materials in massive source rocks are mainly dispersed without preferred orientation.[44] The diagenetic alterations in different rock fabrics of mixed source rocks were examined in the literature.[45] However, the full-scale pore distribution and its relationships with mineral composition and geochemical parameters of the mixed source rocks are still unclear. The aims of this study are as follows: (1) provide a comprehensive analysis of pore structures for mixed source rocks across <10 nm and 10^5 nm by using N_2 adsorption, MICP analysis, and X-ray μCT; (2) investigate the full-scale pore network differences among fine laminae, thick laminae, and massive rock fabric within the Lucaogou mixed source rock system; and (3) clarify the effect of rock fabric, lithofacies, and organic matter on hydrocarbon transport and conduit development. The results obtained in this study offered a new perspective on the resource potential of mixed source rock systems with varied rock fabrics.

2. GEOLOGICAL SETTING

The Junggar Basin is petroliferous in NW China, and it is enclosed by Delun, Halaalt, and Zhayier mountains in the northwest and Kelameili and Qinggelidi mountains in the northeast. The south boundary consists of Bogda and Yilinhebiergen mountains (Figure 1a). Jimusar Sag is a subordinate tectonic unit in the southeast Junggar Basin (Figure 1b). Upon the pre-Carboniferous basement, the sag deposited multiple source rocks in the Carboniferous, Permian, and Jurassic strata (Figure 1c). The Permian Lucaogou Formation is the main source rock in Jimusar Sag. It was deposited in a salty lake environment after the relict sea close-off.[42,45,46] The shale generally has a laminar structure. Specifically, the dark gray-black dolomitic shale of Lucaogou Formation has horizontal laminar fabric, a high proportion of organic matter along with the bedding, deeper lake with a low-energy environment. However, for the silt-bearing massive mudstone, some with disturbance fabric, the organic matter distribution is weakly oriented, usually deposited in the shallow to shore shallow lake environment.[44]

The Permian Lucaogou Formation from Jimusar Sag (Figure 1b) is a hot shale oil resource target.[49−51] The Jimusar Sag (Figure 1b) has been the first national shale oil demonstration area in China in 2020.[52] The sweet-spot intervals from the upper and lower Lucaogou Formation contribute to the majority of shale oil production. Until 2020, a total of 52 vertical wells and 37 horizontal wells have been drilled; among them, the total shale oil production from the 28 production wells is as high as 370 t/d. Typically, the cumulative oil production of well J172 is above 1.9×10^4 t, the average shale oil production is about 4 t/d, and the total shale oil prospective resources in the whole Junggar Basin is 50×10^8 t.[44]

3. SAMPLES AND METHODS

3.1. Samples. In this study, 14 original Lucaogou shale and mudstone samples were selected from 12 vertical wells allocated in the Jimusar Sag (Figure 1b). All these 14 source rock samples are drilled parallel to the core bedding in depth from 1691.4 to 3577.4 m (Table 1). The samples cover the current maturity stage of Lucaogou source rock from immature to the peak oil window. The samples contain thickly laminated, fine laminated, and massive rock fabrics. The limited 14 samples represent the Lucaogou source rocks relatively well with three kinds of rock fabrics. The rock material used for analysis in this study was well preserved whole rock with no sign of weathering or oxidation.

3.2. Methods. The X-ray diffractometer (XRD) analysis of the source rock samples was performed using a Bruker D2 PHASER X-ray diffractometer, which was equipped with a copper X-ray source (30 kV,10 mA) and a scintillation X-ray detector. The emissive and receiving slits of the instrument were 0.6 and 8 mm, respectively. All samples were tested over an angular range of 6−50° with a step size of 0.02° (2θ).[53,54] The source rock samples were used by a Rock-Eval 6 analyzer to get the organic geochemistry parameters. TOC, free hydrocarbon content (S_1), pyrolysis peak temperature (T_{max}), cracking hydrocarbon (S_2), and reflectance (R_o) were obtained.

To study pore structure characteristics at different rock structures in the current oil window, N_2 adsorption, MICP analysis, and X-ray μCT were performed to display full-range pore size distribution (PSD) characteristics. N_2 adsorption was tested by a Micromeritics NOVA 4200e apparatus. Ten shale sample aliquots weighing 3 g were analyzed with N_2 at a bath temperature of 77 K to obtain information about micropores (<10 nm) and transitional pores (10−100 nm in diameter).[14,55] A multi-point Brunauer−Emmett−Teller (BET) model was used to obtain the specific surface area (SSA), and the multi-point Barret−Joyner−Halenda (BJH) model was applied to obtain the pore volume (PV) and the pore size distribution (PSD) of source rock samples. A detailed depiction of the theories and methods can be found in Thommes et al. and Sing et al.[56,57] Mercury intrusion

https://doi.org/10.1021/acs.energyfuels.2c01484
Energy Fuels 2022, 36, 8161−8179

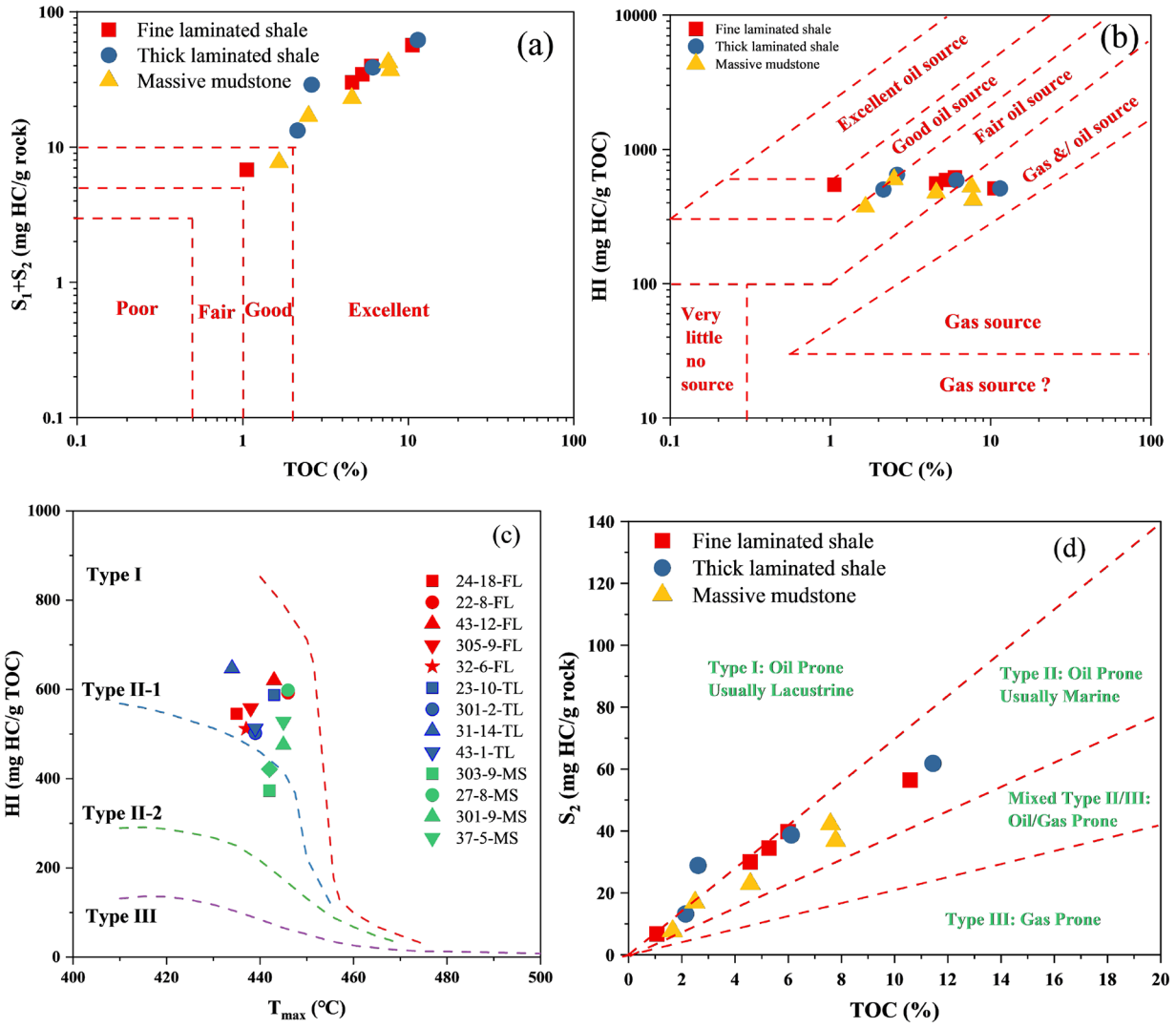

Figure 2. Cross diagrams of (a) TOC vs S_1 + S_2, (b) TOC vs HI, (c) T_{max} vs HI, and (d) TOC vs S_2 of the Lucaogou source rock samples.

(MICP) was tested on a Micromeritics AutoPore IV 9500 instrument. The mercury injection pressure ranged up to 420.58 MPa, which corresponds to mercury injected into a 3 nm pore throat. Pore size distribution (PSD) was calculated from the Washburn equation.[58] 3D pore and throat network topologies were reconstructed by X-ray micro-CT. CT scanning was conducted using a ZEISS Xridia Versa-500 Micro-CT instrument. The resolution of images obtained from all samples was 1.05 μm/voxel. The working electric current and voltage of the X-ray source were 89 μA and 90 kV, respectively. The selected 14 representative core samples used the multiscale CT scanning data and maximum-ball method.[54,59,60] Due to the limited resolution of the equipment, in this study, only macropores (>1.0 μm) were investigated by X-ray μCT. The Avizo 9.0 software (FEI, Hillsboro, OR, USA)[59] was used to process images. The images were processed with a median filter. An interactive thresholding method was used to generate a binarized representative organic matter network. The detailed methodology and procedure of processing X-ray μCT data have been explained in previous studies.[54,60−62]

4. RESULTS

4.1. Organic Geochemistry. TOC and Rock-Eval pyrolysis can identify the source rock quality, organic matter type, thermal maturity, and oil-generating potential.[63] The Rock-Eval results and TOC contents are summarized in Table 1. Source rock with TOC contents at <0.5, 0.5−1, 1−2, 2−4, and >4 wt % can be evaluated as poor, fair, good, very good, and excellent source rock, respectively.[64] The TOC content of 14 source rock samples ranges from 1.06 to 11.44 wt % (mean 5.28 wt %). The TOC content indicates that the Lucaogou source rocks are very good and excellent. When the S_2 value is at >10 and 20 mg HC/g rock, it can be considered as having a very good and excellent hydrocarbon generation potential.[63] Rock-Eval S_1 and S_2 of Lucaogou samples are 1.01−11.99 and 5.77−58.61 mg HC/g rock, respectively. The average S_2 value is 27.98 mg HC/g rock, indicating excellent hydrocarbon generation potential. The source rock samples have the S_1 + S_2 values of 6.78−61.88 mg HC/g rock (mean 31.20 mg HC/g rock). The hydrogen index (HI) differs widely from 373.41 to 647.24 mg HC/g TOC.

The relationship between the TOC content and Rock-Eval S_1 + S_2 shows that all source rock samples are grouped into the zone of good to excellent source rock (Figure 2a). The source rock samples are mainly scattered in the oil zone, and some samples are grouped into the gas/oil zone in the cross plot of TOC content versus hydrocarbon index (Figure 2b). As illustrated in the cross plot of T_{max} versus HI, the 14 source rock samples from the Lucaogou Formation were mainly scattered into the mature oil window of Type I to Type II_1 kerogen (Figure 2c). The plots of S_2 versus TOC content are also widely used to identify the kerogen type.[65] The plot of S_2 versus TOC content shows a

https://doi.org/10.1021/acs.energyfuels.2c01484
Energy Fuels 2022, 36, 8161−8179

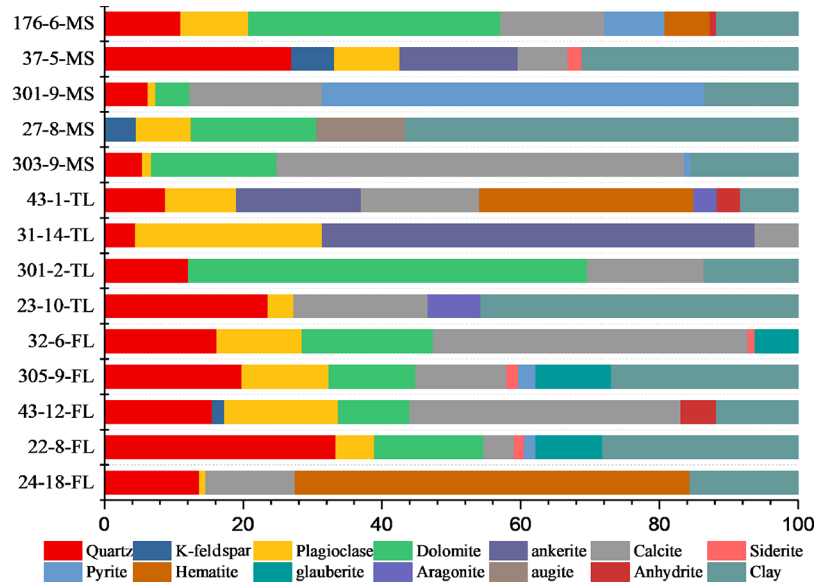

Figure 3. Mineral compositions of Lucaogou source rock samples.

scattered range of variation for both S_2 and TOC. This denotes that type I and type II kerogen are present according to this method (Figure 2d). In addition, both the T_{max} and measured vitrinite reflectance (%R_o) values of the Lucaogou source rock samples are listed in Table 1. T_{max} values range from 435 to 446 °C. The Lucaogou source rock has R_o values of 0.58−0.90% (mean = 0.75%) (Table 1). This indicates that the source rocks have entered the mature stage, and some samples are in the peak oil window. Overall, high TOC contents with high S_2 and HI values indicate that Lucaogou source rock has good quality organic matter for petroleum generation over the current geological age.[63]

4.2. Lithology and Mineralogy. The Lucaogou source rock samples were pulverized into particle sizes less than 300 mesh for XRD analysis to measure the mineral compositions, and the results are plotted in Figure 3. Figure 3 shows that carbonate (dolomite and calcite), clay, quartz, and plagioclase are the primary minerals for the studied source rock samples. Specifically, the carbonate mineral content ranges from 12.9 to 76.1%, with an average of 41.01%. The clay mineral content varies from 8.3 to 56.7% with an average of 23.2%. Meanwhile, the siliceous mineral content (quartz) ranges from 4.5 to 27.0%, with an average of 14.1%. This is inconsistent with the Barnett Shale from the Fort Worth Basin with a higher content of siliceous mineral content. For the economic development of the lacustrine shale system, the content of quartz and carbonate should be higher than 40%, and the clay mineral content should be less than 30%.[66] These results infer that the Lucaogou source rock was deposited in a mixed environment with a high content of carbonate and low content of siliceous minerals (Figure 3). The average brittle mineral content is 69.0%, which is favorable for hydraulic fracturing. This is consistent with the previous study.[67]

In this study, quartz, feldspar, pyrite (QFP), carbonate minerals, clay minerals from XRD data, and OM were used as lithologic identification factors for qualitative analysis. The mineralogy-based ternary classification scheme of source rock proposed by Gamero-Diaz et al.[68] was used to classify the type of mineral facies. TOC contents of 4, 2, and 1% are used as the threshold of high-TOC, medium-TOC, and low-TOC source rock, respectively. As illustrated in Figure 4, the Lucaogou source rock samples mainly belong to high-TOC mixed

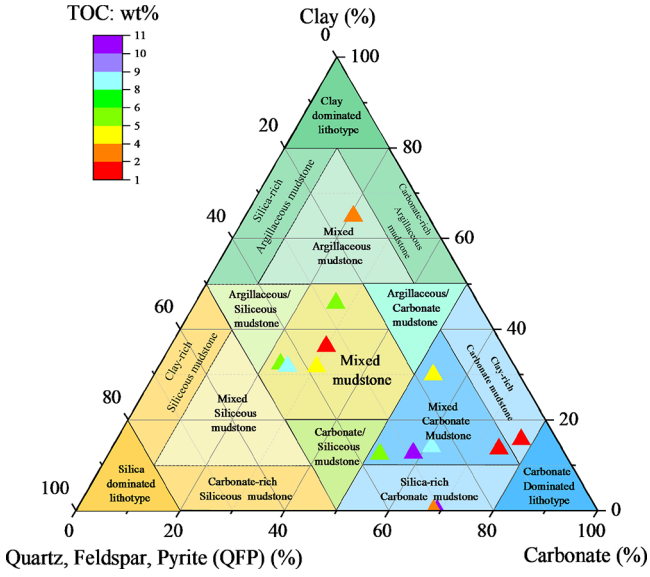

Figure 4. Ternary diagram of the XRD of the identified mineral facies and the terminology and classification for source rock facies.

carbonate mudstone and high-TOC mixed mudstone. Moreover, some samples were also plotted at medium-TOC mixed argillaceous mudstone, high-TOC silica-rich carbonate mudstone, and low-TOC clay-rich carbonate mudstone (Figure 4).

4.3. Pore Structure Analysis of MICP. The MICP test can measure pore volume (PV) through the injected mercury volume and requires only small sample pieces or fragments.[69] Table 2 shows the values of grain density, bulk density, total pore volume, and permeability gained from MICP tests. The MICP experiment shows that the total porosity ranges of samples with fine laminae (FL), thick laminae (TL), and massive (MS) samples are 1.37−4.66%, 2.63−7.32%, and 2.00−8.74%, respectively. The data shows that the permeability of the FL sample, TL sample, and MS samples are 0.367−0.869, 0.099−

https://doi.org/10.1021/acs.energyfuels.2c01484
Energy Fuels 2022, 36, 8161−8179

Table 2. Physical Properties of 10 Source Rock Samples Based on MICP Analysis

sample	grain density (g/cm^3)	bulk density (g/cm^3)	total pore volume (cm^3/g)	total pore area (cm^2/g)	total porosity (%)	permeability (mD)	average pore diameter (nm)
24-18-FL	2.58	2.46	0.019	10.735	4.66	0.480	7.06
43-12-FL	2.42	2.34	0.014	5.243	3.16	0.869	10.28
305-9-Fl	2.47	2.43	0.006	3.344	1.37	0.367	6.72
32-6-FL	2.13	2.09	0.009	4.967	1.86	0.464	7.18
23-10-TL	2.37	2.20	0.033	17.659	7.32	1.407	7.54
31-14-TL	2.66	2.51	0.023	0.982	5.73	0.099	93.12
43-1-TL	2.38	2.31	0.011	6.497	2.63	0.767	7.01
303-9-MS	2.54	2.31	0.038	21.592	8.74	3.017	7.00
301-9-MS	2.47	2.32	0.026	12.293	6.05	1.477	8.50
176-6-MS	2.52	2.47	0.008	4.745	2.00	0.986	6.80

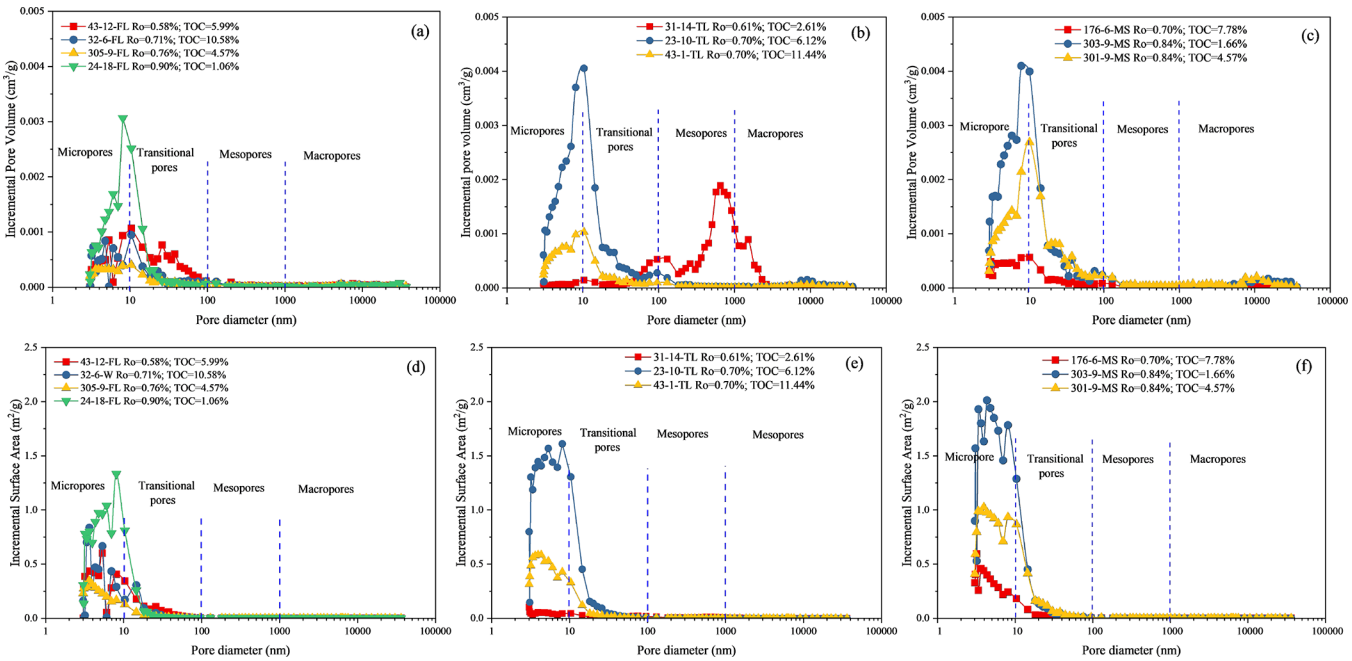

Figure 5. Pore size distribution defined by incremental pore volume for (a) FL shale, (b) TL shale, and (c) MS mudstone samples and surface area of (d) FL shale, (e) TL shale, and (f) MS mudstone samples using mercury injection capillary pressure (MICP) analyses. Pore diameters range between 3 nm and 400 μm. FL: fine laminae, TL: thick laminae, MS: massive.

1.407, and 0.986−3.017 mD. No significant differences in porosity and permeability are observed among samples with varied rock fabrics.

The curves from the incremental pore volume (PV) and pore surface area (SSA) versus pore diameter results perfectly reflect pore network distribution. The pore size distribution parameters obtained from the MICP analysis are between 3 and 36,171 nm covering the micropores, transitional pores, mesopores, and macropores as shown in Figure 5 with the PV and SSA. Overall, all samples used in the mercury experiments mainly present a bimodal correlation at the micropores and transitional pores with pore diameters ranging from 3 to 100 nm and some of the macropores with pore diameters more than 3000 nm (Figure 5).

Previous studies reported that the PV generally presents a positive correlation with the PSD, and there is a negative relationship between SSA and the PSD under the given PV.[70,71] However, for Lucaogou source rock, as the pore size increased from micropores to macropores, the incremental pore volume (PV) decreased. The majority of the total PV is from the micropores (<10 nm) and transitional pores (10−100 nm). These pores contribute to both the majority of PV and SSA for Lucaogou source rocks in the oil window (Figure 5). This specifies that the connected pore network identified from MICP is mainly from micropores and transitional pores. The inconsistency of PSD in different lithofacies and organic matter content indicates a strong heterogeneity of pore networks. A negative correlation between TOC and pore volume was observed for the FL source rocks (Figure 5a). In contrast, for the MS samples, a positive correlation between PV and TOC was observed (Figure 5c).

4.4. Pore Structure Analysis of Gas Adsorption. Low-pressure N_2 adsorption was applied to characterize the micropore (<10 nm) and transitional pore (10−100 nm) structures. The relative volume of nitrogen gas adsorbed under varied relative pressure intervals presents the percentage of pores within the detectable pore size range.[72] According to the IUPAC classification, N_2 adsorption isotherms belong to type IV. This indicates that pores smaller than 50 nm are well-developed.[57] The hysteresis loops of type H2 are well developed and indicate the presence of ink-bottle or polymorphism pores. Furthermore, some samples show unclosed hysteresis loops at relatively low pressures (Figure 6), which is due to micropore swelling or an adsorption effect.[29] In this study, the maximum adsorbed N_2 volumes range from 0.345 to 21.788 cm^3/g, and the

https://doi.org/10.1021/acs.energyfuels.2c01484
Energy Fuels 2022, 36, 8161−8179

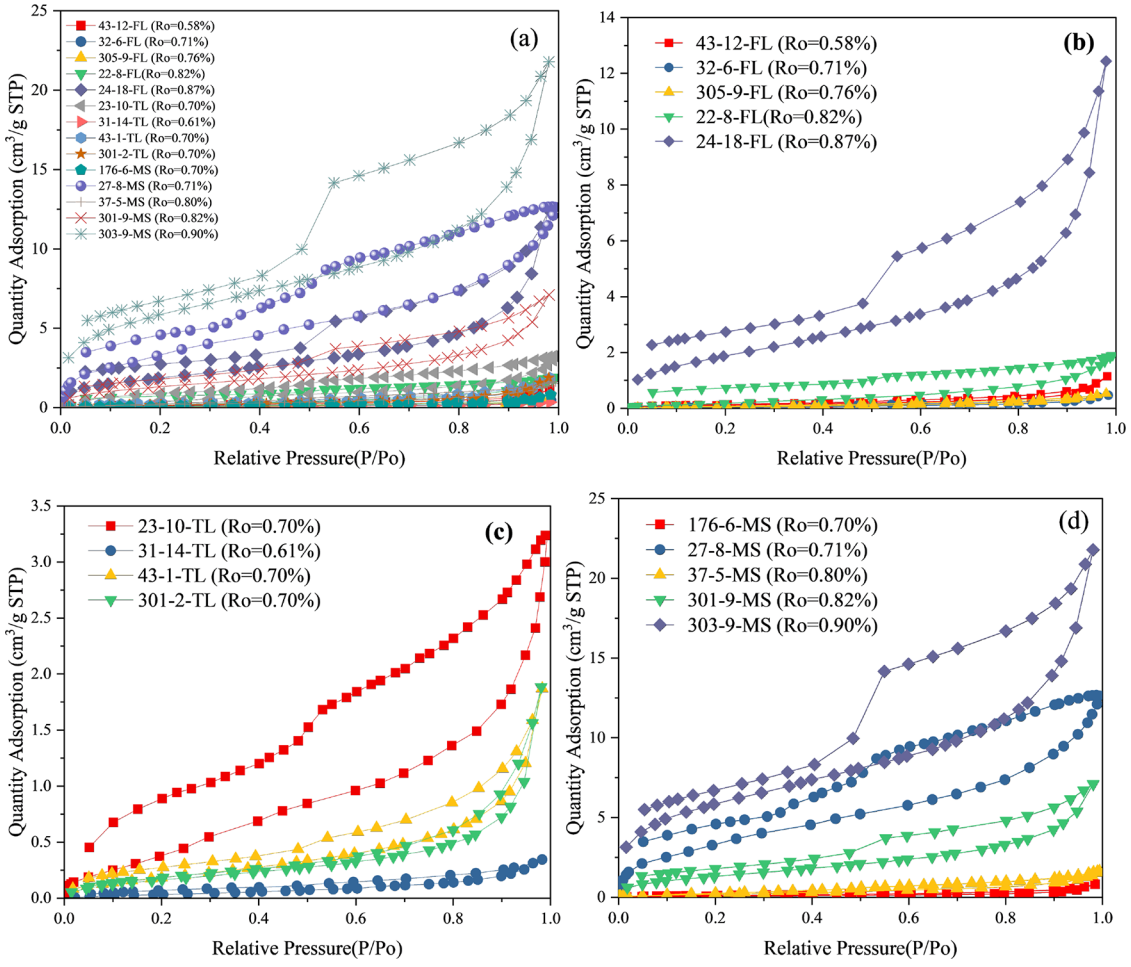

Figure 6. N_2 adsorption isotherms for samples with (a) all samples, (b) fine laminated (FL), (c) thick laminated (TL), and (d) massive (MS) rock fabrics.

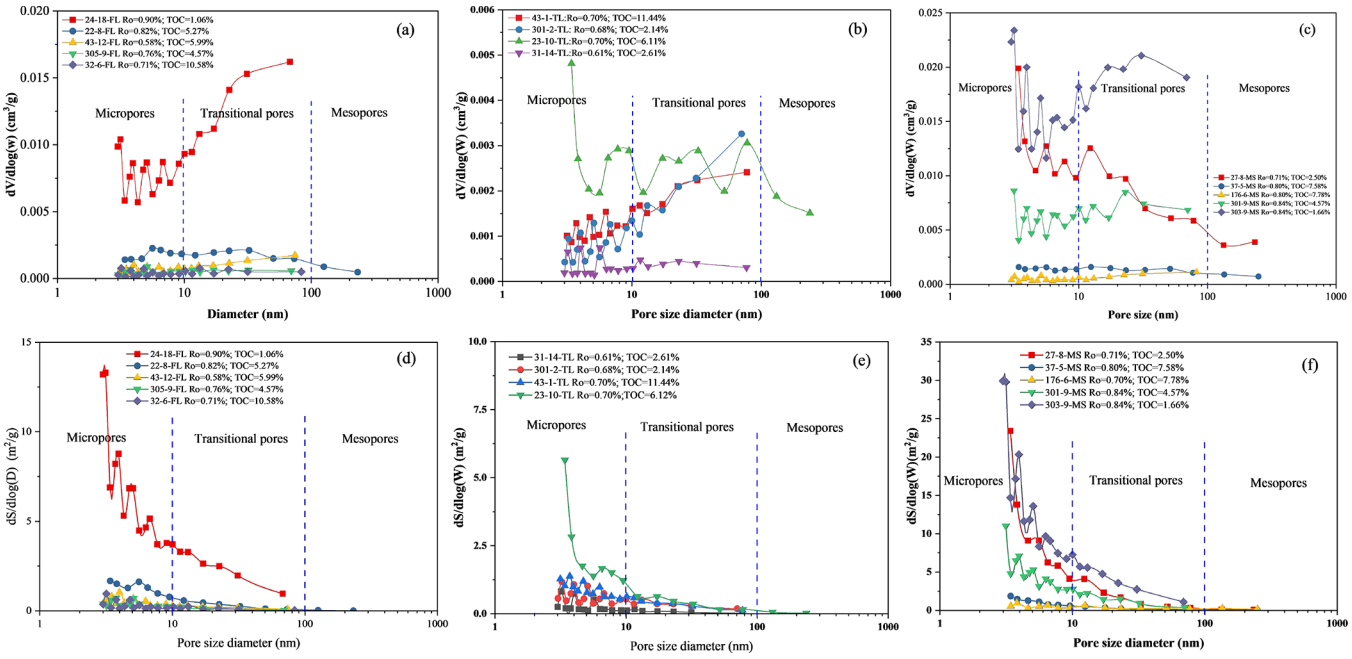

Figure 7. Pore size distribution for samples with log differential of pore volume from (a) fine laminated (FL), (b) thick laminated (TL), and (c) massive (MS) rock fabrics and log differential of pore surface area from (d) fine laminated (FL), (e) thick laminated (TL), and (f) massive (MS) rock fabrics.

https://doi.org/10.1021/acs.energyfuels.2c01484
Energy Fuels 2022, 36, 8161−8179

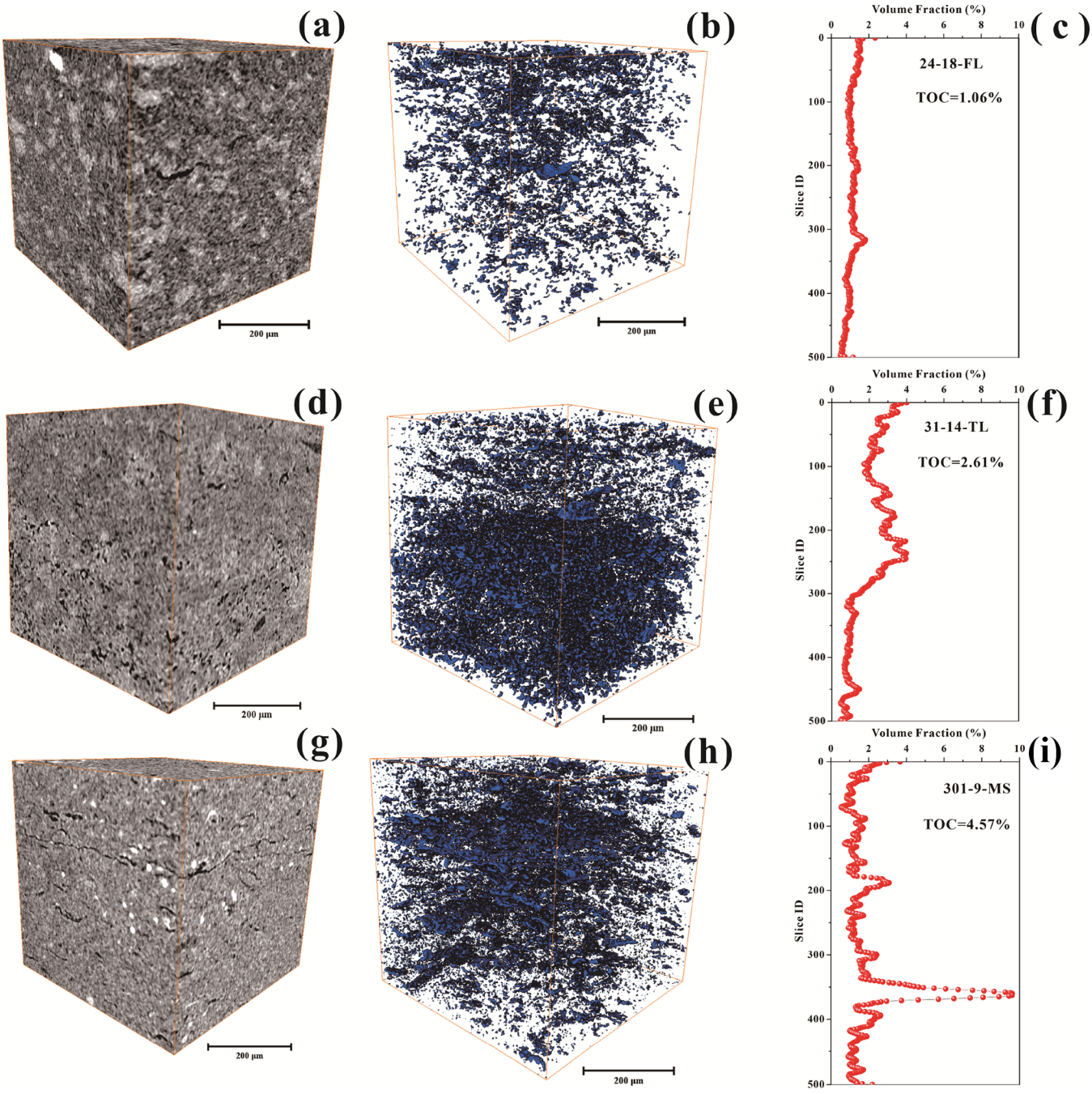

Figure 8. 3D microfracture network of the (a–c) sample 24-18-FL, (d–f) sample 31-14-TL, and (g–i) sample 301-9-MS.

average value is 4.844 cm^3/g. The BET surface areas of the studied source rocks range between 0.17 and 21.49 m^2/g, with an average of 3.73 m^2/g. For FL source rock, the log differential PV presents an increasing pore volume and surface area as the TOC decreases (Figure 7a,d). Similarly, for MS source rock (Figure 7c,f), low-TOC clay-rich carbonate mudstone 303-9-MS presents the highest pore volume and surface area. However, the medium mixed argillaceous mudstone 27-8-MS shows a lower pore volume and surface area. For high-TOC mixed carbonate mudstone 176-6-MS, the PV and SSA decreased to a low level. This indicates that the high content of organic matter might hinder micropore and transitional pore development in FL and MS samples. In contrast, the TOC content from the TL shale samples presents a positive correlation with the pore volume and surface area (Figure 7b,e).

4.5. Pore Structure Analysis of Micro-CT. MICP, gas adsorption, and CT scanning are frequently used laboratory techniques for quantitative evaluation of shale pore structures. The N_2 gas adsorption and MICP are fluid saturation methods. They can detect the interconnected pores at 2–200 and 3–400,000 nm, respectively. As a nondestructive technology, CT scanning provides intuitive pore morphology and quantitative evaluation for pores and throats on a micron-scale (>1 μm). In this study, all 14 samples were examined by X-ray micro-CT, and representative 2D grayscale tomographic images, 3D pore-throat spatial distribution, and porosity at each slice from low-TOC mixed shale 24-18-FL, medium-TOC silica-rich carbonate

https://doi.org/10.1021/acs.energyfuels.2c01484
Energy Fuels 2022, 36, 8161–8179

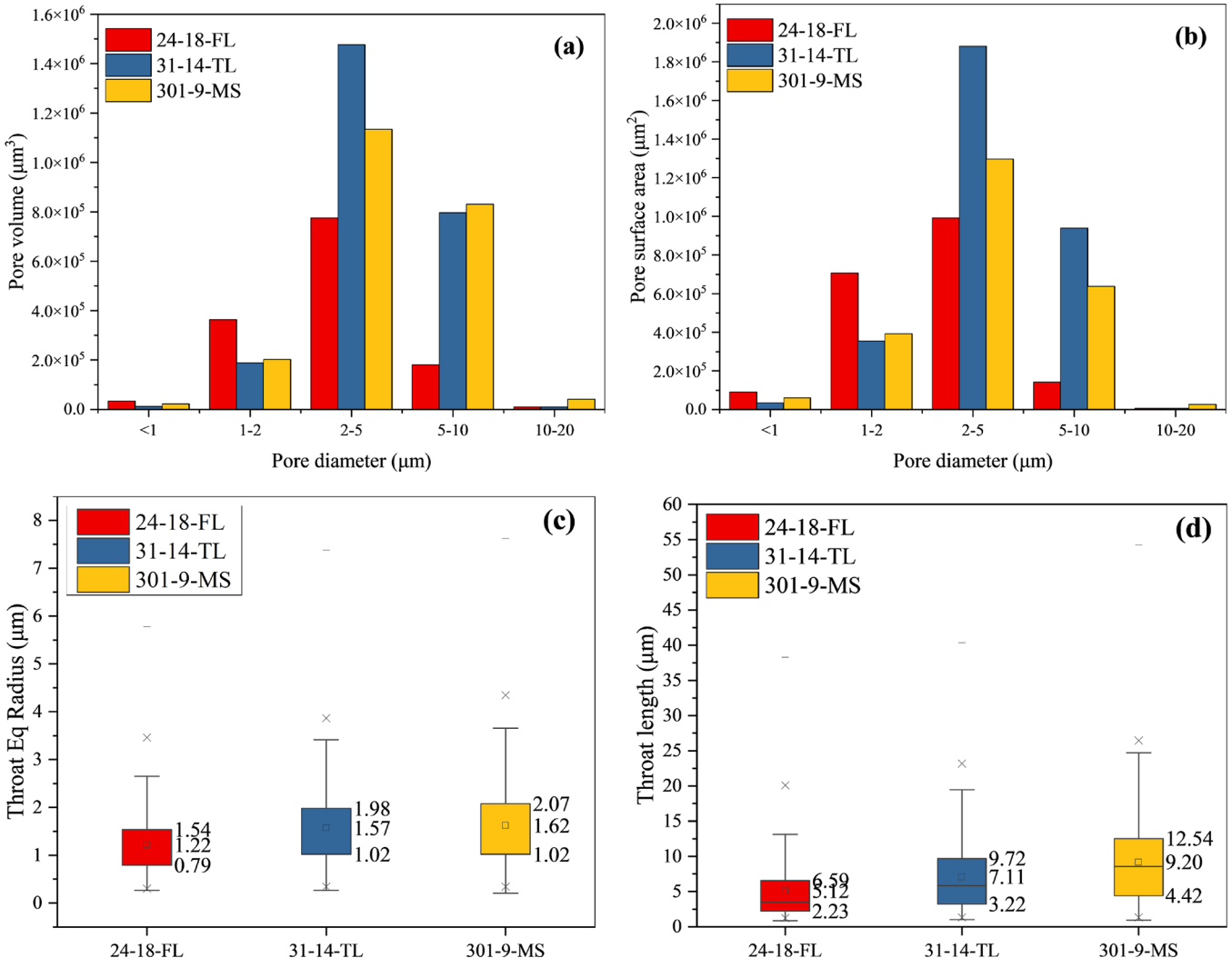

Figure 9. (a) Pore and microfracture volumes and (b) pore surface area, (c) throat radius, and (d) throat length distribution obtained by micro-CT for the Lucaogou source rock 24-18-FL, 23-10-TL, and 301-9-MS.

shale 31-14-TL, and high-TOC mixed carbonate mudstone 301-9-MS are displayed in Figure 8. The 3D visualization results reveal evident differences in the pore system between the three lithofacies of source rock from the Lucaogou Formation. In the low-TOC mixed shale 24-18-FL sample, the microfracture is not well-developed and the fracture length is limited (Figure 8a–c). For medium-TOC silica-rich carbonate shale 31-14-TL, the microfractures are more developed at the carbonate laminae with a distinct higher porosity (Figure 8d–f). For the high-TOC mixed carbonate mudstone 301-9-MS samples, several well-connected microfractures were observed with a slice porosity at 10%. These well-propagated fractures only occurred at high-TOC mudstone. This implies that abundant organic matter might enhance microfracture propagation (Figure 8g–i). Overpressure and volume shrinkage of OM during hydrocarbon generation are the main drivers of microcracking. In the oil window, more solid kerogen in the high TOC source rocks converts into low-density liquid oil, and the fluid volume expansion drives overpressure and creates fractures. Under overpressure, the optimal fracture propagation direction is along the zone where the energy consumption is the least. This is supported by thermal shrinkage fractures at the boundary between organic matter and inorganic minerals (Figure 8g,h).

In 3D space, most pores are isolated with poor connectivity. Figure 9 shows the relationship between the micro-CT pore volume and pore diameter. With increasing pore size, the volume of macropores (>1 μm) first increases and then decreases. At 2–5 μm, both the macropore volume and surface area achieve their peak values (Figure 9a,b). The morphology of the pores varies from spherical to irregular, in which ink-bottle-shaped pores are most developed (Figure 8b,e). Some elongated and jagged curves microfractures are observed, and the average fracture length is between 3.12 and 9.20 μm. The throat equal radius is between 1.22 and 1.66 μm (Figure 9c,d).

The comprehensive comparison between multiscale pores is significant and applicable. Lei et al.[36] combined the data from gas adsorption, MICP, NMR, and CT scanning into different scales according to the order of magnitude. First, the vertical coordinates should be unified into pore volume per unit of mass. Take sample 24-18-FL as an example. Based on micro-CT scanning and the 3D reconstruction data, the macropore PV with 0.78–10.59 μm from 24-18-FL is 1.36×10^6 μm^3. The volume results detected from the micro-CT 3D dataset (cubic with side length at 500 μm) is 1.25×10^8 μm^3. The measured source rock density is 2.457 g/cm^3, and the mass of the micro-CT 3D dataset is calculated to be 3.07×10^{-2} g. The pore

https://doi.org/10.1021/acs.energyfuels.2c01484
Energy Fuels 2022, 36, 8161–8179

Table 3. Macropore (>1 μm) Volume Distribution from Different Ranges of PSD for All Lucaogou Source Rocks

sample	lithofacies	R_o (%)	TOC (wt %)	<1 μm (cm^3/g)	1−2 μm (cm^3/g)	2−5 μm (cm^3/g)	5−10 μm (cm^3/g)	10−20 μm (cm^3/g)
22-8-FL	mixed shale	0.82	5.27	4.73×10^{-5}	3.79×10^{-4}	1.60×10^{-3}	5.47×10^{-4}	0.00×10^{0}
43-12-FL	mixed carbonate shale	0.58	5.99	4.45×10^{-5}	5.26×10^{-4}	2.42×10^{-3}	1.04×10^{-3}	2.14×10^{-5}
305-9-FL	mixed shale	0.76	4.57	2.69×10^{-5}	3.51×10^{-4}	2.12×10^{-3}	1.60×10^{-3}	3.93×10^{-4}
32-6-FL	silica-rich carbonate shale	0.71	10.58	7.16×10^{-5}	9.25×10^{-4}	7.65×10^{-3}	8.02×10^{-3}	6.78×10^{-4}
24-18-FL	mixed shale	0.90	1.06	1.10×10^{-4}	1.18×10^{-3}	2.52×10^{-3}	5.88×10^{-4}	3.21×10^{-5}
301-2-TL	mixed carbonate shale	0.70	2.14	8.48×10^{-5}	6.26×10^{-4}	8.98×10^{-4}	8.75×10^{-4}	1.63×10^{-4}
43-1-TL	mixed carbonate shale	0.70	11.44	1.15×10^{-4}	1.62×10^{-3}	7.49×10^{-3}	1.23×10^{-3}	0.00×10^{0}
23-10-TL	mixed shale	0.70	6.12	8.28×10^{-5}	7.84×10^{-4}	2.53×10^{-3}	1.50×10^{-3}	8.37×10^{-5}
31-14-TL	silica-rich carbonate shale	0.61	2.61	3.99×10^{-5}	6.11×10^{-4}	4.80×10^{-3}	2.59×10^{-3}	3.39×10^{-5}
301-9-MS	mixed carbonate mudstone	0.84	4.57	7.77×10^{-5}	6.96×10^{-4}	3.91×10^{-3}	2.87×10^{-3}	1.43×10^{-4}
176-6-MS	mixed carbonate mudstone	0.70	7.78	3.66×10^{-5}	4.07×10^{-4}	2.56×10^{-3}	1.15×10^{-3}	2.27×10^{-5}
303-9-MS	clay-rich carbonate mudstone	0.90	1.66	9.95×10^{-5}	8.55×10^{-4}	2.67×10^{-3}	1.15×10^{-3}	1.54×10^{-5}
27-8-MS	mixed argillaceous mudstone	0.71	2.50	1.52×10^{-4}	1.40×10^{-3}	1.97×10^{-3}	4.52×10^{-4}	0.00×10^{0}
37-5-MS	mixed mudstone	0.80	7.58	7.78×10^{-5}	7.82×10^{-4}	2.34×10^{-3}	1.50×10^{-3}	0.00×10^{0}

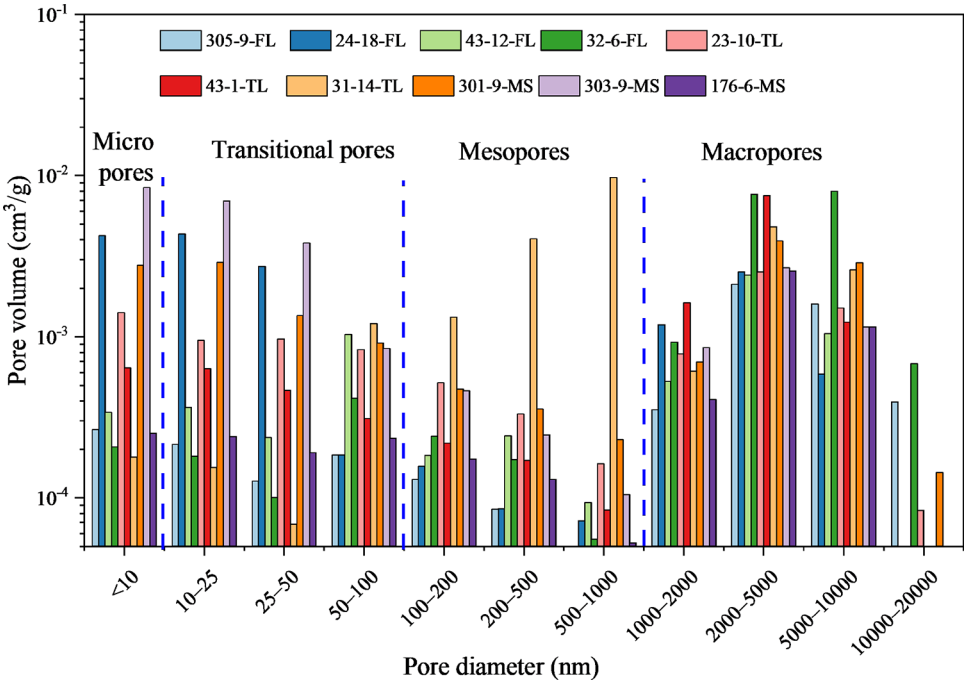

Figure 10. Correlation between multiscale pore volume and pore size distribution combined with N_2 adsorption, MICP, and micro-CT. FL: fine laminae, TL: thick laminae, and MS: massive rock fabric.

(fracture) volume (0.78−10.59 μm) of the unit mass source rock samples is 4.44×10^{-5} cm^3/g. The detailed calculation description is referred to Guo et al.[73] The macropore volume for all the source rock samples is listed in Table 3. Overall, based on statistical data from micro-CT, the micron-scale pore space is mainly supplied by macropores and microfractures at 1−10 μm.

5. DISCUSSION

5.1. Full-Scale Pore-Fracture Distribution in the Mixed Lucaogou Source Rock. Depending on the mixed sedimentary environment, complex mineral fabric, varied TOC, and pore types, the source rock pore-fracture structures are different. In the current study, the range of PSD measured using multiple methods was between 2 and 10^5 nm. The micropore (<10 nm), transitional pore (10−100 nm), mesopore (100−1000 nm), and macropore (>1000 nm) are quantified in the Lucaogou Formation source rocks based on measured PSD data from N_2 adsorption (<50 nm), MICP (50−1000 nm), and micro-CT scanning (>1000 nm). The calculation method follows Guo et al.[73] and Lei et al.[36] For example, the unit mass values of micropore, transition pore, mesopore, and macropore (fractures) volumes of sample 43-12-FL are 3.39×10^{-4}, 1.63×10^{-3}, 5.19×10^{-4}, and 4.00×10^{-3} cm^3/g, respectively. The unit mass values of micropore, transition pore, mesopore, and macropore (microfracture) surface areas are 2.51×10^{-1}, 5.42×10^{-2}, 3.29×10^{-3}, and 1.17×10^{-3} m^2/g, respectively. Figures 10 and 11 illustrate the full-scale pore size distribution of 10 source rock samples from the Lucaogou Formation.

The results display that the average percentage values of pore volume for micropores, transitional pores, mesopores, and macropores (fracture) are 11.14, 21.62, 10.77, and 56.47%, respectively (Figure 10). Overall, for Lucaogou source rock, the transitional pore and macropore (fracture) contribute the majority of pore volume, and the contribution from the micropore and mesopore is limited (Table 4). Moreover, the pore surface areas for micropores, transitional pores, mesopores,

https://doi.org/10.1021/acs.energyfuels.2c01484
Energy Fuels 2022, 36, 8161−8179

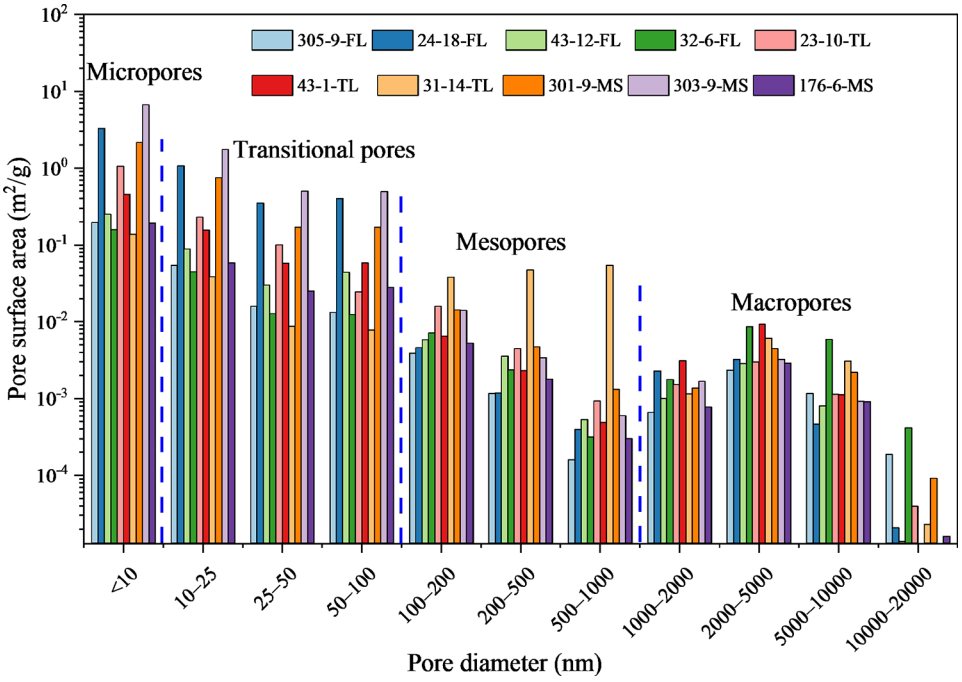

Figure 11. Correlation between the multiscale pore surface area and pore size distribution combined with N_2 adsorption, MICP, and micro-CT. FL: fine laminae, TL: thick laminae, and MS: massive rock fabric.

and macropores are of 62.45, 30.45, 5.47, and 1.63%, respectively (Figure 11). This indicates that the majority surface area of Lucaogou source rock is from micropores and transitional pores. The surface area is an indicator of adsorption capacity in porous media. A higher surface area implies a larger adsorption space,[73] indicating that the oil in micropores and transitional pores are mainly in the adsorbed phase. The low oil fluidity in these pores has been supported by molecular dynamic simulation.[74] Fortunately, more than half of the pore volume is from macropores and micron fractures (Figure 10). This pore network distribution is beneficial for oil transport and storage.

Shale oil is mainly stored in the pore-fracture networks as free and adsorbed oil.[74] The adsorbed oil content has a stronger correlation with the micropore content, while the occurrence space for the free oil is primarily related to large intra- and intergranular pores and fractures in the micron scale.[67,75] In this study, the average micropore (<10 nm) volume of the Lucaogou source rock is 0.00187 cm^3/g, accounting for about 11.14% of the total pore volume and 62.45% of the total specific surface area of the source rocks. However, the average micron-scale macropore (Figure 12a,b) and fracture (>1000 nm) (Figure 12c) volume is 0.00698cm^3/g, accounting for about 56.47% of pore volume and 1.63% of the total specific surface area of source rocks, indicating great potential for free oil accumulation. The free and adsorbed oil content are indicators of varied adsorption capacity among organic matter and non-organic mineral components. Accordingly, the organic matter (Figure 12b,d) shows the strongest adsorption capacity for oil followed by clay minerals (Figure 12d), quartz (Figure 12c), and calcite.[76] The results in this study are significant to the comprehensive understanding of pore-fracture network development in the mixed lacustrine source rock system.

5.2. Relationship between Organic Matter and Mineral Content. The mineral composition plays a significant role in hydrocarbon retention and generation.[67] Quartz in the Devonian shales and Longmaxi shale are biogenic origins as supported by the positive relationship between quartz and TOC content.[70,77] However, the Lucaogou source rock was deposited in a mixed lacustrine environment, and both quartz and terrigenous clast present a weak-medium unimodal correlation with the TOC content (Figure 13a,b). When TOC increased to 6%, the terrigenous clast and quartz mineral contents reached their peak at around 30 and 20%, respectively. This implies that the origin of quartz is mixed with both terrigenous and biogenic origins. A negative relationship between TOC and terrigenous clastic minerals from marine lower Silurian Longmaxi shale indicates the organic matter was diluted by terrigenous clastic material.[78] For Lucaogou source rock, when TOC is higher than 6%, the dilution effect of terrigenous detrital input on organic matter becomes stronger as indicated by decreasing trends of both quartz and terrigenous mineral contents (Figure 13a,b). Moreover, the quartz content shows a medium positive role with clay minerals (Figure 13c). For Lucaogou source rock in Santanghu Basin, a negative correlation between carbonate minerals and TOC was observed, and it was attributed to the dilution of carbonate minerals.[79] However, for Lucaogou source rock in the Junggar Basin, no apparent correlation was observed between TOC, HI, and carbonate minerals (Figure 13d). This signifies that carbonate mineral plays a limited role in organic matter deposition and generation potential. For the Lucaogou source rocks, a slight increase in hydrogen index (HI) was observed with increasing terrigenous clast and clay minerals, especially when the clay minerals are more than 20% (Figure 13e,f). This indicates that both terrigenous clast and clay mineral control the source rock hydrocarbon generation potential for mixed Lucaogou source rocks.

5.3. Effect of Mineral Contents on Pore Structures. When the carbonate mineral content is less than 45%, a negative correlation was observed between carbonate and micropore (<10 nm) and transitional pore (10−100 nm) volume (Figure 14a). However, when the carbonate increases from 45 to 80%, the carbonate presents a positive relationship with pore volume

https://doi.org/10.1021/acs.energyfuels.2c01484
Energy Fuels 2022, 36, 8161−8179

Table 4. Volume Content of Different Types of Pores (Unit: cm^3/g)

pore size (nm)	pore type	43-12-FL	305-9-FL	32-6-FL	24-18-FL	43-1-TL	23-10-TL	31-14-TL	301-9-MS	176-6-MS	303-9-MS
<10	micropore	3.39×10^{-4}	2.64×10^{-4}	2.07×10^{-4}	4.23×10^{-3}	6.40×10^{-4}	1.41×10^{-3}	1.79×10^{-4}	2.77×10^{-3}	2.51×10^{-4}	8.43×10^{-3}
10−25	transitional pore	3.64×10^{-4}	2.15×10^{-4}	1.81×10^{-4}	4.33×10^{-3}	6.32×10^{-4}	9.48×10^{-4}	1.54×10^{-4}	2.89×10^{-3}	2.40×10^{-4}	6.97×10^{-3}
25−50	transitional pore	2.37×10^{-4}	1.27×10^{-4}	1.00×10^{-4}	2.73×10^{-3}	4.63×10^{-4}	9.69×10^{-4}	6.83×10^{-5}	1.35×10^{-3}	1.91×10^{-4}	3.80×10^{-3}
50−100	transitional pore	1.03×10^{-3}	1.84×10^{-4}	4.13×10^{-4}	1.84×10^{-4}	3.10×10^{-4}	8.31×10^{-4}	1.20×10^{-3}	9.14×10^{-4}	2.35×10^{-4}	8.44×10^{-4}
100−200	mesopore	1.83×10^{-4}	1.30×10^{-4}	2.41×10^{-4}	1.57×10^{-4}	2.18×10^{-4}	5.17×10^{-4}	1.32×10^{-3}	4.71×10^{-4}	1.74×10^{-4}	4.60×10^{-4}
200−500	mesopore	2.43×10^{-4}	8.48×10^{-5}	1.72×10^{-4}	8.56×10^{-5}	1.70×10^{-4}	3.31×10^{-4}	4.04×10^{-3}	3.54×10^{-4}	1.30×10^{-4}	2.46×10^{-4}
500−1000	mesopore	9.34×10^{-5}	2.65×10^{-5}	5.52×10^{-5}	7.17×10^{-5}	8.38×10^{-5}	1.62×10^{-4}	9.74×10^{-3}	2.30×10^{-4}	5.26×10^{-5}	1.04×10^{-4}
1000−2000	macropores	5.26×10^{-4}	3.51×10^{-4}	9.25×10^{-4}	1.18×10^{-3}	1.62×10^{-3}	7.84×10^{-4}	6.11×10^{-4}	6.96×10^{-4}	4.07×10^{-4}	8.55×10^{-4}
2000−5000	macropores	2.42×10^{-3}	2.12×10^{-3}	7.65×10^{-3}	2.52×10^{-3}	7.49×10^{-3}	2.53×10^{-3}	4.80×10^{-3}	3.91×10^{-3}	2.56×10^{-3}	2.67×10^{-3}
5000−10,000	macropores	1.04×10^{-3}	1.60×10^{-3}	8.02×10^{-3}	5.88×10^{-4}	1.23×10^{-3}	1.50×10^{-3}	2.59×10^{-3}	2.87×10^{-3}	1.15×10^{-3}	1.15×10^{-3}
10,000−20,000	macropores	2.14×10^{-5}	3.93×10^{-4}	6.78×10^{-4}	3.21×10^{-5}	0.00×10^{0}	8.37×10^{-5}	3.39×10^{-5}	1.43×10^{-4}	2.27×10^{-5}	1.54×10^{-5}

(Figure 14a). There is no apparent relationship between the carbonate content and transitional pore (100−1000 nm) and macropore (>1000 nm) volume (Figure 14b). For the terrigenous clast minerals, both micropore and transitional pore volume decreased when terrigenous clast mineral is between 5 and 35%; this suggests that the terrigenous matrix input hindered the micropore and transitional pore development (Figure 14c), while the mesopores (100−1000 nm) and macropores (>1000 nm) are not affected by terrigenous contents in this study (Figure 14d). The origin of this phenomenon is likely associated with diagenetic alteration. In Lucaogou Formation, the terrigenous clastic particles are rock fragments, quartz, and feldspar. The authigenic quartz might occupy the dissolution pores in feldspars, and the euhedral microcrystalline quartz cement in mixed layers of smectite/illite also decreases the micropore and transitional pore volume.[45,80] The clay mineral presents a distinct effect on pore volume with varied pore size distribution. When clay mineral content is at 15%, the peak pore volume for micropores, transitional pores, and mesopores is observed for Lucaogou source rock (Figure 14e), and the macropore volume presents a decreasing evolution trend with clay mineral increased from 0 to 30% and shows a slight increase from 30 to 40% (Figure 14f). Overall, for mixed source rock from Lucaogou Formation, the carbonate mineral shows an "up concave" type relationship with the micropore and transitional pore volume, and terrigenous clast mineral exhibits a negative impact on micropore and transitional pore volume. The clay mineral plays a negative role in macropore development.

5.4. Effect of Organic Matter on Pore Structures. The previous study shows that during the late oil window, the low-TOC (<5.5%) shale presents a positive trend between TOC and porosity. However, for high-TOC (>5.5%) shale, there is a weak or no relationship in porosity with arising TOC content.[81] This indicates that for the high maturity Marcellus shale (R_o 1.0−2.1%), TOC plays a stronger role in OM-hosted pore development than thermal maturity.[81] However, in this study, for mixed lacustrine source rock in the oil window, TOC presents a medium negative relationship with porosity and no apparent relationship with permeability (Figure 15a,b). This indicates that the OM-hosted pore system is not well developed and TOC plays a complex role in full-scale pore network development. Specifically, the TOC content plays a medium negative role in micropore (<10 nm) and transitional pore (10−100 nm) volume (Figure 15c,d), indicating that the ductile organic matter might foster intense compaction, and the generated hydrocarbon might clog the mineral interstices in the range less than 100 nm.[17,82] However, as the TOC content increases from low TOC (<2 wt %) to high TOC (>4 wt %), the macropore volume starts to increase at a high rate (Figure 15f). This suggests that a productive source rock system should comprise sufficient organic matter to support a percolating network, and abundant hydrocarbon volume expansion might trigger micron fracture development (Figure 12b,c). The organic matter content shows no relationship with mesopore (100−1000 nm) volume (Figure 15e). The lack of correlation between TOC and mesopore volume suggests that organic matter is not the main pore space contribution at 100−1000 nm.

5.5. Effect of Rock Fabric on Shale Oil Potential and Pore Structures. Jarvie et al.[83] used the oil saturation index (OSI = S_1/TOC × 100) to evaluate the shale oil potential and defined that when OSI > 100 mg HC/g TOC, the source rock reached the threshold recoverable oil value. Jin et al.[84] reported that high-TOC laminated shale retains a higher content of free

https://doi.org/10.1021/acs.energyfuels.2c01484
Energy Fuels 2022, 36, 8161−8179

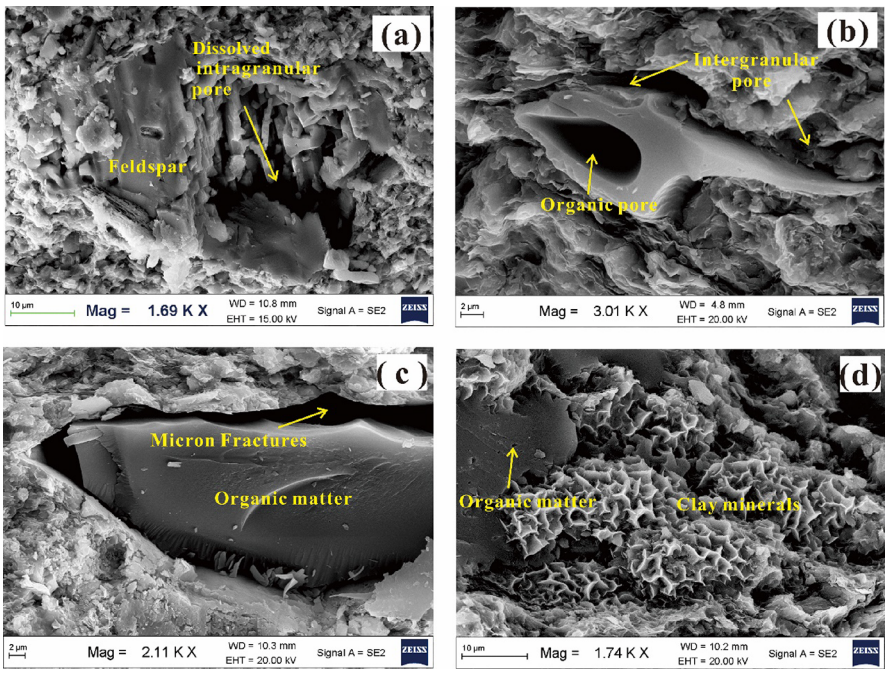

Figure 12. SEM micrographs of pore types and petrological characteristics of the samples from Lucaogou Formation. (a) Dissolved intragranular pore. (b) Organic matter pore and intergranular pore. (c) Microfracture. (d) Organic matter and clay minerals.

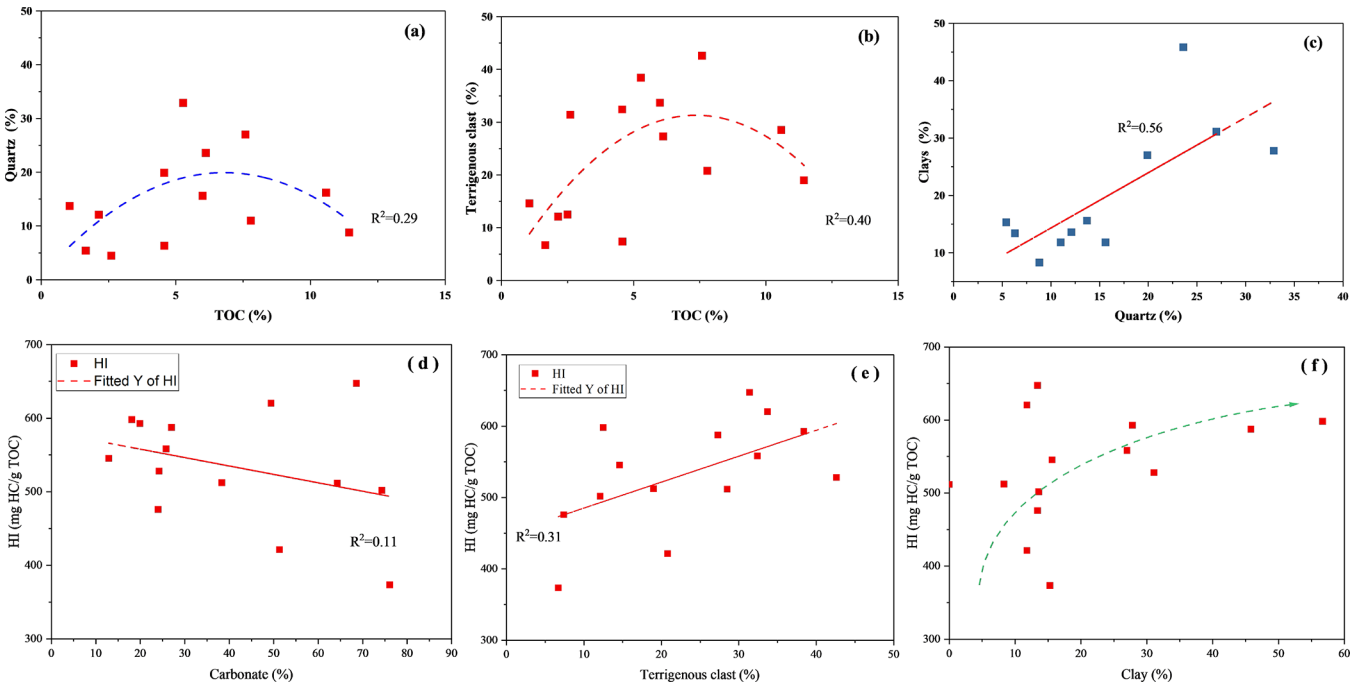

Figure 13. Cross plots of (a) quartz vs TOC; (b) terrigenous clast vs TOC; (c) quartz vs clay; (d) carbonate vs HI; (e) terrigenous clast vs HI; and (f) clay vs HI for Lucaogou source rock samples. TOC: total organic carbon. HI: hydrogen index.

oil than mudstone. However, for Lucaogou source rock samples with TL, FL, and MS rock fabric, only shale (301-2-TL) with medium-TOC thick laminated fabric has OSI > 100 mg HC/g TOC (Figure 16a). The majority of Lucaogou source rock contains OSI less than 100 mg HC/g TOC. Moreover, no apparent difference in OSI was observed among FL, TL, and MS source rocks. Interestingly, a negative relationship between TOC and OSI was also observed for all mixed source rock samples (Figure 16a). This indicates that the effect of rock fabric on shale oil potential is negligible compared with organic matter abundance (Figure 16a).

The discrepancy in rock composition and organic matter quality between laminated shale and massive mudstone determines their contributions to shale oil resources.[44] Based on N_2 adsorption, MICP, and micro-CT analysis, it is remarkable that compared with MS mudstone, FL and TL shales possess similar total pore volume. However, the detailed pore volume distribution is different between shale and mudstone. Specifically, the macropores and fractures are

https://doi.org/10.1021/acs.energyfuels.2c01484
Energy Fuels 2022, 36, 8161−8179

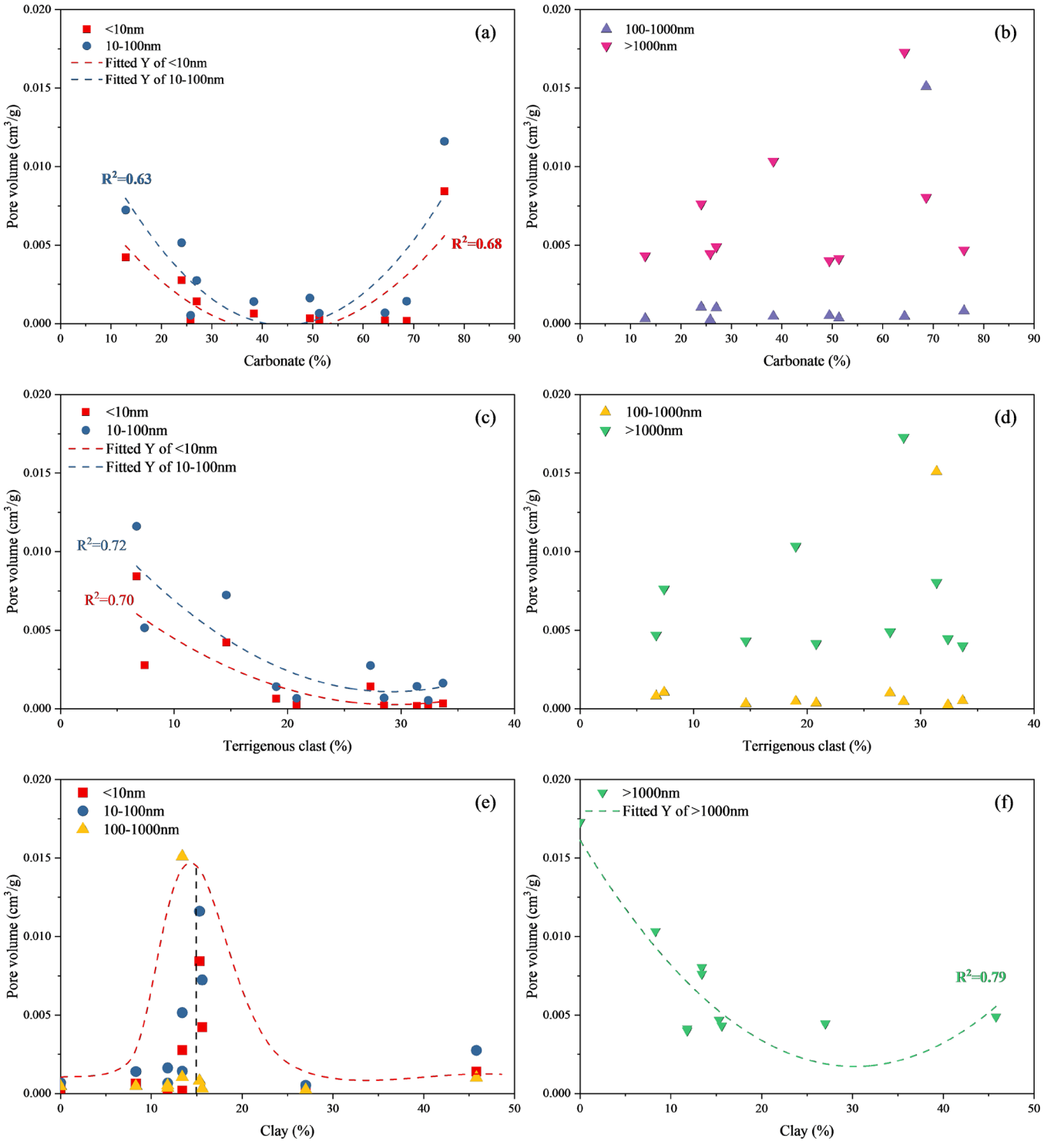

Figure 14. Relationship between minerals and pore volume. (a) Carbonate vs micropore and transitional pore volume. (b) Carbonate vs mesopore and macropore volume. (c) Terrigenous clast vs micropore and transitional pore volume. (d) Terrigenous clast vs mesopore and macropore volume. (e) Clay vs micropore, transitional pore, and mesopore volume. (f) Clay vs macropore volume.

relatively more developed in laminated shale (Figure 16b,c), especially in TL shale samples (Figure 16c). In contrast, for massive mudstone, the micropores, transitional pores, and macropores are relatively more developed than mesopores (Figure 16d). For Lucaogou source rock in Jimusar Sag, the micropore (<10 nm) and transitional pore (10−100 nm) volume in laminated shale are smaller than those in mudstone (Figure 16b−d). This is controlled by pore morphology with slit-like pores in laminated shale and plate-like and ink-bottle pores in mudstone.[85]

With the same rock fabric, the organic matter and lithofacies can influence pore-fracture network development. For the FL shale, high-TOC mixed carbonate shale (43-12-FL) and mixed shale (305-9-FL) present relatively higher macropore volumes. The high-TOC silica-rich carbonate shale (32-6-FL) contains the highest macropore volume, and this might contribute to its

https://doi.org/10.1021/acs.energyfuels.2c01484
Energy Fuels 2022, 36, 8161−8179

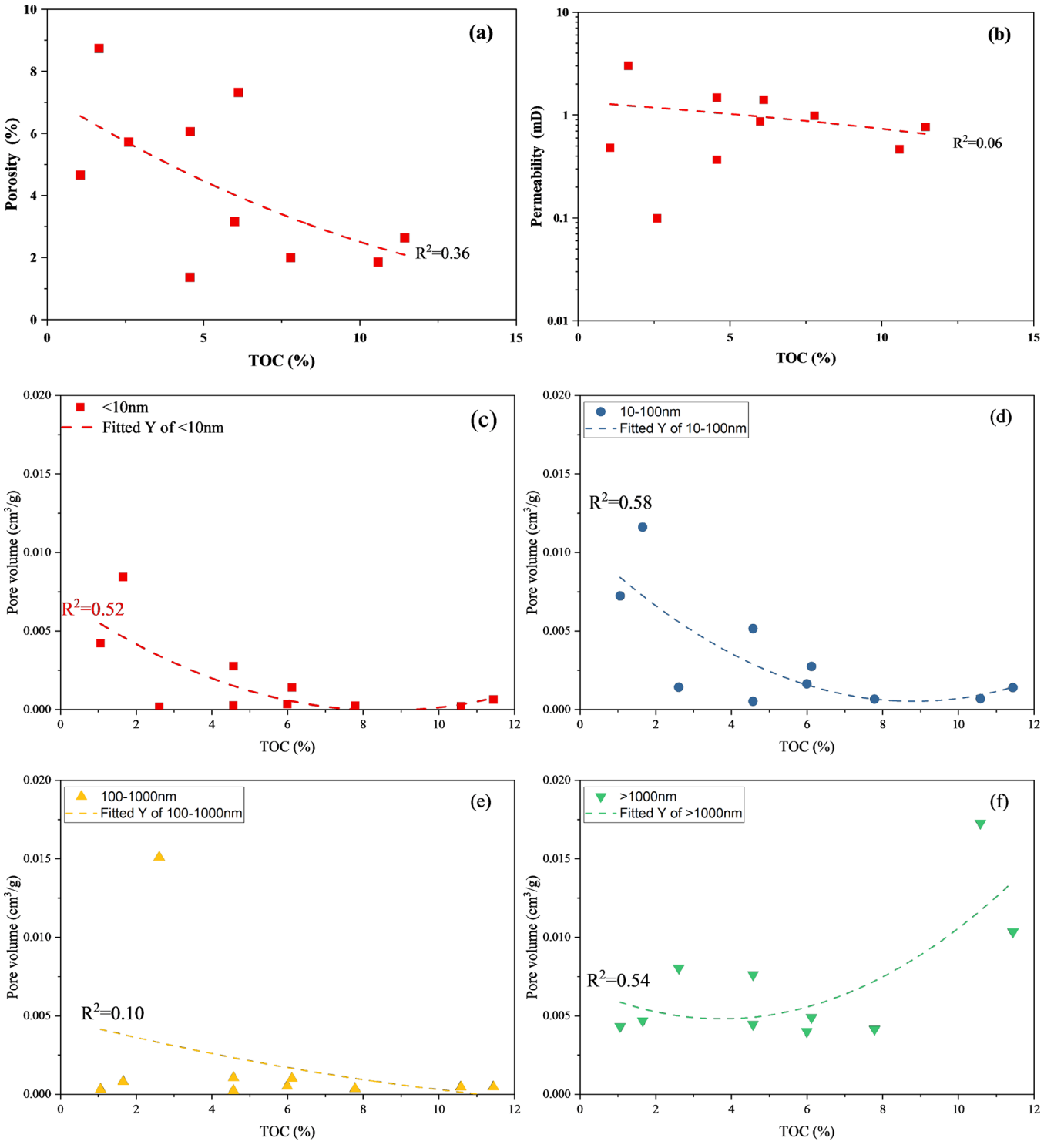

Figure 15. Total organic matter (TOC, wt %) versus measured (a) bulk porosity and (b) permeability of MICP measurement and relationship between TOC and (c) micropores (<10 nm), (d) transitional pores (10−100 nm), (e) mesopores (100−1000 nm), and (f) macropores (>1000 nm) from Lucaogou source rocks.

high TOC content (Figure 15f). In contrast, the mixed shale (24-18-FL) presents a relatively higher micropore and transitional pore volume corresponding to its clay content at 15.6% (Figure 14e). For the TL shale, the medium-TOC silica-rich carbonate shale (31-14-TL) (Figure 16c) presents the highest pore volume. This implies that shales with thick parallel laminae and medium-TOC content possess favorable shale oil potential.

Being influenced by the mixed sedimentary environment, the source rock pore structures are diverse. Here, using a combination of multiscale experimental methods, the full-scale PSD of Lucaogou source rocks is characterized. The macropores (>1 μm) and transitional pores (100−100 nm) contribute to the majority of the pore volume. This is significant in the uptick in oil production from mixed lacustrine source rock systems. Apart from geochemical restraints on the shale pore network, the

https://doi.org/10.1021/acs.energyfuels.2c01484
Energy Fuels 2022, 36, 8161−8179

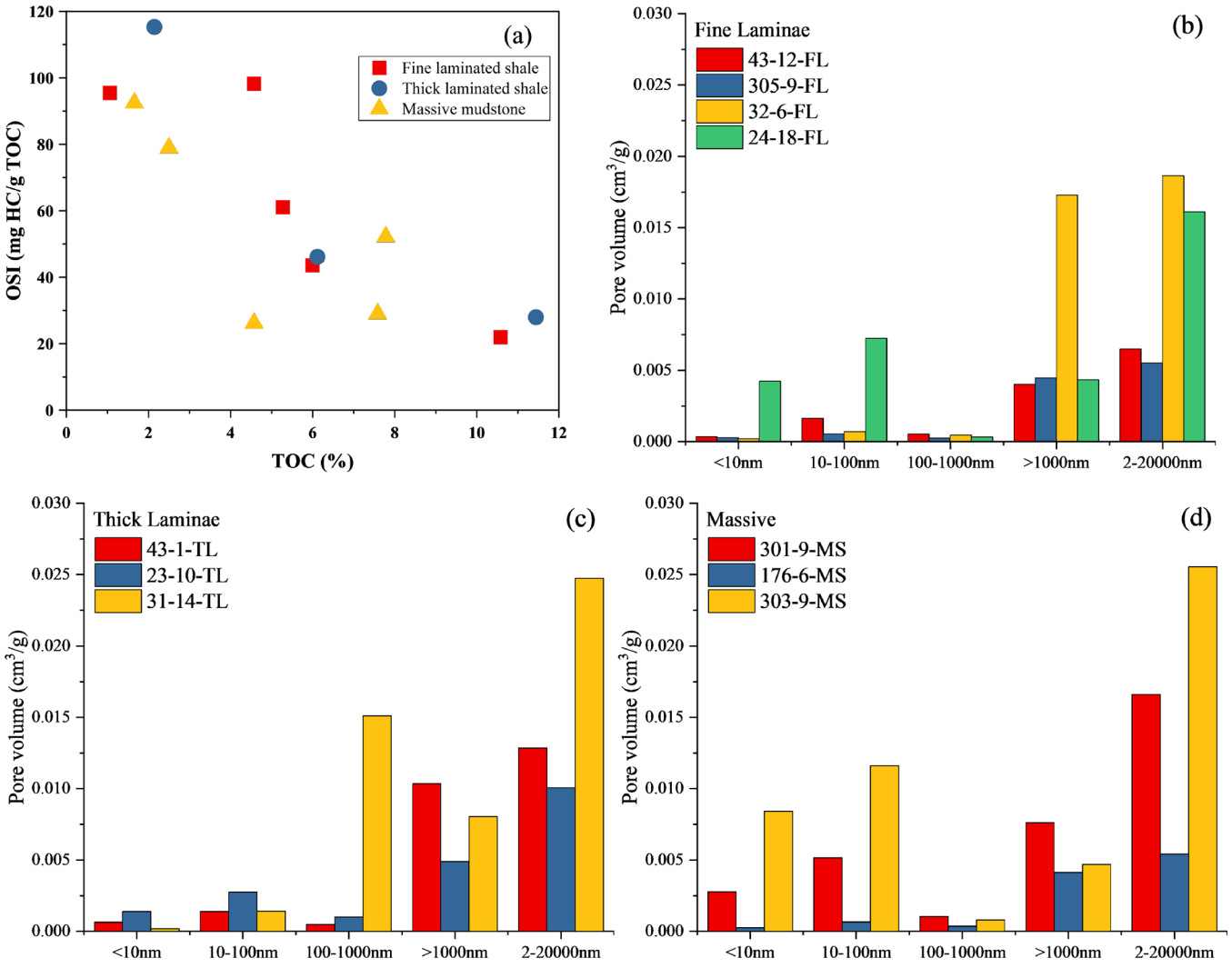

Figure 16. Differences among source rock with FL, TL, and MS rock fabric on (a) TOC vs OSI; (b) pore volume bar charts of shale with fine laminae; (c) pore volume bar charts of shale with thick laminae; and (d) pore volume bar charts of mudstone with massive fabric. TOC: total organic carbon, OSI: oil saturation index, FL: fine laminae, TL: thick laminae, MS: massive.

results obtained in this study clarify the effect of rock fabric, and lithofacies on PSD, this provides a new perspective on the resource potential of mixed source rock systems with varied rock fabrics.

6. CONCLUSIONS

The main findings of this study are concluded as follows:

1. The Lucaogou source rocks contain mainly type I and type II kerogen and show good to excellent hydrocarbon generation potential. The mixed Lucaogou source rock contains a high content of carbonate and a low content of siliceous minerals, showing a higher content of brittle minerals.
2. The full-scale pore-fracture distribution shows that the average percentage values of pore volume for micropores (<10 nm), transitional pores (10−100 nm), mesopores (100−1000 nm), and macropores (fracture) (>1000 nm) are 11.14, 21.62, 10.77, and 56.47%, respectively. However, the average percentage values of pore surface area for the abovementioned pores are 62.45, 30.45, 5.47, and 1.63%, respectively.
3. There exists a distinct feature between laminated and massive rock fabric. For the micropores and transitional pores, the SSA and BJH PV of FLS and TLS are lower than MS. However, macropores and microfracture are more developed in samples with laminae rock fabric than with massive fabric. A negative relationship between TOC and OSI was also observed for all mixed source rocks.
4. The micropore (<10 nm) and transitional pore (10−100 nm) volumes in laminated shale are smaller than those in mudstone. Shales with thick parallel laminae and medium-TOC content possess favorable shale oil potential.

AUTHOR INFORMATION

Corresponding Authors

Jianhui Zeng − *State Key Laboratory of Petroleum Resources and Prospecting and College of Geosciences, China University of Petroleum (Beijing), Beijing 102249, China;* orcid.org/0000-0003-4768-043X; Email: zengjh@cup.edu.cn

Juncheng Qiao − *State Key Laboratory of Petroleum Resources and Prospecting and College of Geosciences, China University*

https://doi.org/10.1021/acs.energyfuels.2c01484
Energy Fuels 2022, 36, 8161−8179

of Petroleum (Beijing), Beijing 102249, China;
Email: Juncheng.Qiao@cup.edu.cn

Authors

Guangqing Yang − *State Key Laboratory of Petroleum Resources and Prospecting and College of Geosciences, China University of Petroleum (Beijing), Beijing 102249, China*

Yazhou Liu − *State Key Laboratory of Petroleum Resources and Prospecting and College of Geosciences, China University of Petroleum (Beijing), Beijing 102249, China*

Shengnan Liu − *State Key Laboratory of Petroleum Resources and Prospecting and College of Geosciences, China University of Petroleum (Beijing), Beijing 102249, China; SINOPEC Shengli Oilfield Company, Dongying 257022, China*

Wanting Jia − *State Key Laboratory of Petroleum Resources and Prospecting and College of Geosciences, China University of Petroleum (Beijing), Beijing 102249, China; CNPC Engineering Technology R&D Company Limited, Beijing 102206, China*

Weifu Cao − *Exploration and Development Research Institute, PetroChina Daqing Oilfield Company, Daqing 163712, China*

Chengyun Wang − *Exploration and Development Research Institute, PetroChina Huabei Oilfield Company, Renqiu 062552, China*

Feng Geng − *State Key Laboratory of Petroleum Resources and Prospecting and College of Geosciences, China University of Petroleum (Beijing), Beijing 102249, China*

Wenfei Wei − *State Key Laboratory of Petroleum Resources and Prospecting and College of Geosciences, China University of Petroleum (Beijing), Beijing 102249, China*

Complete contact information is available at:
https://pubs.acs.org/10.1021/acs.energyfuels.2c01484

Notes

The authors declare no competing financial interest.

■ ACKNOWLEDGMENTS

The authors sincerely thank the Experimental Center of Exploration and Development Research Institute of PetroChina Xinjiang Oilfield Company for their convenience in data and sample collection. This work was financially supported by the National Natural Science Foundation of China (grant no. 41972147).

■ REFERENCES

(1) Yu, H.; Xu, H.; Fu, W.; Lu, X.; Chen, Z.; Qi, S.; Wang, Y.; Yang, W.; Lu, J. Extraction of shale oil with supercritical CO_2: Effects of number of fractures and injection pressure. *Fuel* **2021**, *285*, No. 118977.

(2) Huang, C.; Hou, H.; Yu, G.; Zhang, L.; Hu, E. Energy solutions for producing shale oil: Characteristics of energy demand and economic analysis of energy supply options. *Energy* **2020**, *192*, No. 116603.

(3) Li, Y.; Yang, J.; Pan, Z.; Meng, S.; Wang, K.; Niu, X. Unconventional natural gas accumulations in stacked deposits: A discussion of upper Paleozoic coal-bearing strata in the east margin of the Ordos Basin, China. *Acta Geol. Sin. (Engl. Ed.)* **2019**, *93*, 111−129.

(4) Li, Y.; Yang, J.; Pan, Z.; Tong, W. Nanoscale pore structure and mechanical property analysis of coal: An insight combining AFM and SEM images. *Fuel* **2020**, *260*, No. 116352.

(5) Zhang, Y.; Zeng, J.; Dai, Z.; Viswanathan, H.; Xiao, T.; Ma, Y.; Feng, X. Experimental investigation on oil migration and accumulation in tight sandstones. *J. Pet. Sci. Eng.* **2018**, *160*, 267−275.

(6) Takbiri-Borujeni, A.; Kazemi, M.; Liu, S.; Zhong, Z. Molecular simulation of enhanced oil recovery in shale. *Energy Procedia* **2019**, *158*, 6067−6072.

(7) Wu, S.; Zhai, X.; Yang, Z.; Bale, H.; Hong, Y.; Cui, J.; Pan, S.; Lin, S. Characterization of fracture formation in organic-rich shales-An experimental and real time study of the Permian Lucaogou Formation, Junggar Basin, northwestern China. *Mar. Pet. Geol.* **2019**, *107*, 397−406.

(8) Hoffman, B. T. Comparison of various gases for enhanced recovery from shale oil reservoirs. *Soc. Pet. Eng.* **2012**, *2*, 1−8.

(9) Elwegaa, K.; Emadi, H.; Soliman, M.; Gamadi, T.; Elsharafi, M. Improving oil recovery from shale oil reservoirs using cyclic cold carbon dioxide injection−An experimental study. *Fuel* **2019**, *254*, 115586.

(10) Mahzari, P.; Mitchell, T. M.; Jones, A. P.; Oelkers, E. H.; Striolo, A.; Iacoviello, F.; Shearing, P. R.; Juri, J. E. Novel laboratory investigation of Huff-n-Puff gas injection for shale oils under realistic reservoir conditions. *Fuel* **2021**, *284*, No. 118950.

(11) Wang, L.; Tian, Y.; Yu, X.; Wang, C.; Yao, B.; Wang, S.; Winterfeld, P. H.; Wang, X.; Yang, Z.; Wang, Y.; Cui, J.; Wu, Y.-S. Advances in improved/ enhanced oil recovery technologies for tight and shale reservoirs. *Fuel* **2017**, *210*, 425−445.

(12) Zeng, T.; Miller, C. S.; Mohanty, K. K. Combination of a chemical blend with CO_2 Huff-n-Puff for enhanced oil recovery in oil shales. *J. Pet. Sci. Eng.* **2020**, *194*, No. 107546.

(13) Espitalié, J.; Madec, M.; Tissot, B. Role of mineral matrix in kerogen pyrolysis: Influence on petroleum generation and migration. *AAPG Bull.* **1980**, *64*, 59−66.

(14) Li, Y.; Wang, Z.; Pan, Z.; Niu, X.; Yu, Y.; Meng, S. Pore structure and its fractal dimensions of transitional shale: A cross-section from east margin of the Ordos Basin, China. *Fuel* **2019**, *241*, 417−431.

(15) Teng, J.; Deng, H.; Liu, B.; Chen, W.; Fu, M.; Xia, Y.; Yu, H. Insights of the pore system of lacustrine shales from immature to late mature with the aid of petrology, mineralogy and porosimetry: A case study of the Triassic Yanchang Formation of the Ordos Basin, North China. *J. Pet. Sci. Eng.* **2021**, *196*, No. 107631.

(16) Zhang, K.; Lai, J.; Bai, G.; Pang, X.; Ma, X.; Qin, Z.; Zhang, X.; Fan, X. Comparison of fractal models using NMR and CT analysis in low permeability sandstones. *Mar. Pet. Geol.* **2020**, *112*, No. 104069.

(17) Valenza, J. J., II; Drenzek, N.; Marques, F.; Pagels, M.; Mastalerz, M. Geochemical controls on shale microstructure. *Geology* **2013**, *41*, 611−614.

(18) Shi, J.; Jin, Z.; Liu, Q.; Zhang, T.; Fan, T.; Gao, Z. Laminar characteristics of lacustrine organic-rich shales and their significance for shale reservoir formation: A case study of the Paleogene shales in the Dongying Sag, Bohai Bay Basin, China. *J. Asian Earth Sci.* **2022**, *223*, No. 104976.

(19) Lazar, O. R.; Bohacs, K. M.; Macquaker, J. H. S.; Schieber, J.; Demko, T. M. Capturing key attributes of fine-grained sedimentary rocks in outcrops, cores, and thin sections: Nomenclature and description guidelines. *J. Sediment. Res.* **2015**, *85*, 230−246.

(20) Sang, Q.; Zhao, X.; Liu, Y.; Li, Z.; Dong, M. Effects of the laminated-structure and mixed wettability on the oil/water relative permeabilities and oil productions in shale oil formations. *J. Pet. Sci. Eng.* **2022**, *208*, No. 109457.

(21) Li, T.; Jiang, Z.; Su, P.; Zhang, X.; Chen, W.; Wang, X.; Ning, C.; Wang, Z.; Xue, Z. Effect of laminae development on pore structure in the lower third member of the Shahejie Shale, Zhanhua Sag, Eastern China. *Interpretation* **2020**, *8*, T103−T114.

(22) Zou, C.; Pan, S.; Horsfield, B.; Yang, Z.; Hao, S.; Liu, E.; Zhang, L. Oil retention and intrasource migration in the organic-rich lacustrine Chang 7 shale of the upper Triassic Yanchang Formation, Ordos Basin, Central China. *AAPG Bull.* **2019**, *103*, 2627−2663.

(23) Abu-mahfouz, I. S.; Cartwright, J.; Idiz, E.; Hooker, J. N.; Robinson, S. A. Silica diagenesis promotes early primary hydrocarbon migration. *Geology* **2020**, *48*, 483−487.

(24) Xi, K.; Li, K.; Cao, Y.; Lin, M.; Niu, X.; Zhu, R.; Wei, X.; You, Y.; Liang, X.; Feng, S. Laminae combination and shale oil enrichment patterns of Chang 73 sub-member organic-rich shales in the Triassic Yanchang Formation, Ordos Basin, NW China. *Pet. Explor. Dev.* **2020**, *47*, 1342−1353.

(25) Lei, Y.; Luo, X.; Wang, X.; Zhang, L.; Jiang, C.; Yang, W.; Yu, Y.; Cheng, M.; Zhang, L. Characteristics of silty laminae in Zhangjiatan

Shale of southeastern Ordos Basin , China: Implications for shale gas formation. *AAPG Bull.* **2015**, *99*, 661−687.
(26) Xie, X.; Krooss, B. M.; Littke, R.; Amann-hildenbrand, A.; Li, M.; Li, Z.; Snowdon, L. R.; Mohnhoff, D. Accessibility and mobility of hydrocarbons in lacustrine shale: Solvent flow-through extraction experiments on Eocene oil shales from Bohai Bay Basin, eastern China. *Org. Geochem.* **2019**, *127*, 23−36.
(27) Liang, C.; Cao, Y.; Liu, K.; Jiang, Z.; Wu, J.; Hao, F. Diagenetic variation at the lamina scale in lacustrine organic-rich shales : Implications for hydrocarbon migration and accumulation. *Geochim. Cosmochim. Acta* **2018**, *229*, 112−128.
(28) Cao, Z.; Liu, G.; Zhan, H.; Li, C.; You, Y.; Yang, C.; Jiang, H. Pore structure characterization of Chang-7 tight sandstone using MICP combined with N_2GA techniques and its geological control factors. *Sci. Rep.* **2016**, *6*, 36919.
(29) Mastalerz, M.; Schimmelmann, A.; Drobniak, A.; Chen, Y. Porosity of Devonian and Mississippian New Albany Shale across a maturation gradient: Insights from organic petrology, gas adsorption, and mercury intrusion. *AAPG Bull.* **2013**, *97*, 1621−1643.
(30) Zhang, Y.; Zeng, J.; Qiao, J.; Feng, X.; Wang, F.; Ren, N. Experimental study on natural gas migration and accumulation mechanism in sweet spots of tight sandstones. *J. Nat. Gas Sci. Eng.* **2016**, *36*, 669−678.
(31) Yang, Z.; Zou, C.; Wu, S.; Lin, S.; Pan, S.; Niu, X.; Men, G.; Tang, Z.; Li, G.; Zhao, J.; Jia, X. Formation, distribution and resource potential of the "Sweet Areas (Sections)" of continental shale oil in China. *Mar. Pet. Geol.* **2019**, *102*, 48−60.
(32) Li, Y.; Tang, D.; Elsworth, D.; Xu, H. Characterization of coalbed methane reservoirs at multiple length scales: A cross-section from southeastern Ordos Basin, China. *Energy Fuels* **2014**, *28*, 5587−5595.
(33) Li, Y.; Wang, Y.; Wang, J.; Pan, Z. Variation in Permeability during CO_2−CH_4 displacement in coal seams: Part 1 − Experimental insights. *Fuel* **2020**, *263*, No. 116666.
(34) Li, Y.; Zhang, C.; Tang, D.; Gan, Q.; Niu, X.; Wang, K.; Shen, R. Coal pore size distributions controlled by the coalification process: An experimental study of coals from the Junggar, Ordos and Qinshui Basins in China. *Fuel* **2017**, *206*, 352−363.
(35) Zhao, S.; Li, Y.; Wang, Y.; Ma, Z.; Huang, X. Quantitative study on coal and shale pore structure and surface roughness based on atomic force microscopy and image processing. *Fuel* **2019**, *244*, 78−90.
(36) Lei, J.; Pan, B.; Guo, Y.; Fan, Y. F.; Xue, L.; Deng, S.; Zhang, L.; Ruhan, A. A comprehensive analysis of the pyrolysis effects on oil shale pore structures at multiscale using different measurement methods. *Energy* **2021**, *227*, No. 120359.
(37) Tao, S.; Zhao, X.; Tang, D.; Deng, C.; Meng, Q.; Cui, Y. A model for characterizing the continuous distribution of gas storing space in low-rank coals. *Fuel* **2018**, *233*, 552−557.
(38) Zhang, S.; Cao, Y.; Liu, K.; Jahren, J.; Xi, K.; Zhu, R.; Yang, T.; Cao, X.; Wang, W. Characterization of lacustrine mixed fine-grained sedimentary rocks using coupled chemostratigraphic-petrographic analysis: A case study from a tight oil reservoir in the Jimusar Sag, Junggar Basin. *Mar. Pet. Geol.* **2019**, *99*, 453−472.
(39) Song, M.; Liu, H.; Wang, Y.; Liu, Y. Enrichment rules and exploration practices of Paleogene shale oil in Jiyang Depression , Bohai Bay Basin, China. *Pet. Explor. Dev.* **2020**, *47*, 242−253.
(40) Carroll, A. R.; Bohacs, K. M. Lake-type controls on petroleum source rock potential in nonmarine basins. *AAPG Bull.* **2001**, *85*, 1033−1053.
(41) Bohacs, K. M.; Carroll, A. R.; Neal, J. E.; Mankiewicz, P. J. Lake-basin type, source potential, and hydrocarbon character : An integrated sequence-stratigraphic- geochemical framework. *AAPG Bull.* **2000**, *46*, 3−34.
(42) Zhang, J.; Liu, G.; Cao, Z.; Tao, S.; Felix, M.; Kong, Y.; Zhang, Y. Characteristics and formation mechanism of multi-source mixed sedimentary rocks in a saline lake, a case study of the Permian Lucaogou Formation in the Jimusaer Sag, Northwest China. *Mar. Pet. Geol.* **2019**, *102*, 704−724.
(43) Liu, B.; Wang, H.; Fu, X.; Bai, Y.; Bai, L.; Jia, M.; He, B. Lithofacies and depositional setting of a highly prospective lacustrine shale oil succession from the Upper Cretaceous Qingshankou Formation in the Gulong sag, northern Songliao Basin, northeast China. *AAPG Bull.* **2019**, *103*, 405−432.
(44) Zhao, W.; Zhu, R.; Hu, S.; Hou, L.; Wu, S. Accumulation contribution differences between lacustrine organic-rich shales and mudstones and their significance in shale oil evaluation. *Pet. Explor. Dev.* **2020**, *47*, 1160−1171.
(45) Lin, M.; Xi, K.; Cao, Y.; Liu, Q.; Zhang, Z.; Li, K. Petrographic features and diagenetic alteration in the shale strata of the Permian Lucaogou Formation, Jimusar Sag, Junggar Basin. *J. Pet. Sci. Eng.* **2021**, *203*, No. 108684.
(46) Kuang, L.; Tang, Y.; Lei, D.; Chang, Q.; Ouyang, M.; Hou, L.; Liu, D. Formation conditions and exploration potential of tight oil in the Permian saline lacustrine dolomitic rock, Junggar Basin, NW China. *Pet. Explor. Dev.* **2012**, *39*, 700−711.
(47) Cao, Z.; Liu, G.; Zhan, H.; Kong, Y.; Niu, Z.; Zhao, D. Geological control factors of micro oil distribution in tight reservoirs. *Mar. Pet. Geol.* **2016**, *77*, 1193−1205.
(48) Huang, H.; Gao, Y.; Jones, M. M.; Tao, H.; Carroll, A. R.; Ibarra, D. E.; Wu, H.; Wang, C. Astronomical forcing of middle Permian terrestrial climate recorded in a large paleolake in northwestern China. *Palaeogeogr., Palaeoclimatol., Palaeoecol.* **2020**, *550*, No. 109735.
(49) Zhang, C.; Zhu, D.; Luo, Q.; Liu, L.; Liu, D.; Yan, L.; Zhang, Y. Major factors controlling fracture development in the Middle Permian Lucaogou Formation tight oil reservoir, Junggar Basin, NW China. *J. Asian Earth Sci.* **2017**, *146*, 279−295.
(50) Cao, Z.; Liu, G.; Meng, W.; Wang, P.; Yang, C. Origin of different chlorite occurrences and their effects on tight clastic reservoir porosity. *J. Pet. Sci. Eng.* **2018**, *160*, 384−392.
(51) Kuang, L.; Wang, Z.; Feng, C.; Zhao, P.; Mao, R.; Yu, J. Predicting oil saturation of shale-oil reservoirs using nuclear magnetic resonance logs. *Interpretation* **2020**, *8*, SL35−SL43.
(52) Zhao, Z.; Hou, L.; Luo, X.; Sun, F.; Lin, S.; Zhang, L. Total scanning fluorescence characteristics and implications of shale oil in the Lucaogou Formation, Jimsar Sag, Junggar Basin, NW China. *Front. Earth Sci.* **2021**, *9*, No. 664330.
(53) Zhang, J.; Liu, G.; Torsaeter, O.; Tao, S.; Jiang, M.; Li, G.; Zhang, S. Pore-throat structure characteristics and its effect on flow behavior in Gaotaizi tight siltstone reservoir, Northern Songliao Basin. *Mar. Pet. Geol.* **2020**, *122*, No. 104651.
(54) Qiao, J.; Zeng, J.; Jiang, S.; Zhang, Y.; Feng, S.; Feng, X.; Hu, H. Insights into the pore structure and implications for fluid flow capacity of tight gas sandstone : A case study in the upper Paleozoic of the Ordos Basin. *Mar. Pet. Geol.* **2020**, *118*, No. 104439.
(55) Whitelaw, P.; Uguna, C. N.; Stevens, L. A.; Meredith, W.; Snape, C. E.; Vane, C. H.; Moss-Hayes, V.; Carr, A. D. Shale gas reserve evaluation by laboratory pyrolysis and gas holding capacity consistent with field data. *Nat. Commun.* **2019**, *10*, 1−10.
(56) Thommes, M.; Kaneko, K.; Neimark, A. V.; Olivier, J. P.; Rodriguez-Reinoso, F.; Rouquerol, J.; Sing, K. S. W. Physisorption of gases, with special reference to the evaluation of surface area and pore size distribution (IUPAC Technical Report). *Pure Appl. Chem.* **2015**, *87*, 25−25.
(57) Sing, K. S. W.; Everett, D. H.; Haul, R. A. W.; Moscou, L.; Pierotti, R. A.; Rouquérol, J.; Siemieniewska, T. Reporting physisorption data for gas/solid systems—with special reference to the determination of surface area and porosity. *Pure Appl. Chem.* **1985**, *57*, 603−619.
(58) Washburn, E. W. The dynamics of capillary flow. *Phys. Rev.* **1921**, *17*, 273−283.
(59) Saif, T.; Lin, Q.; Butcher, A. R.; Bijeljic, B.; Blunt, M. J. Multi-scale multi-dimensional microstructure imaging of oil shale pyrolysis using X-ray micro-tomography, automated ultra-high resolution SEM, MAPS Mineralogy and FIB-SEM. *Appl. Energy* **2017**, *202*, 628−647.
(60) Gafurova, D.; Kalmykov, A.; Korost, D.; Kalmykov, G. Macropores generation in the Domanic formation shales : Insights from pyrolysis experiments. *Fuel* **2021**, *289*, No. 119933.
(61) Dong, H.; Blunt, M. J. Pore-network extraction from micro-computerized-tomography images. *Phys. Rev. E.* **2009**, *80*, No. 036307.

https://doi.org/10.1021/acs.energyfuels.2c01484
Energy Fuels 2022, 36, 8161−8179

(62) Zhang, Y.; Liu, L.; Wang, D.; Zhang, Z.; Li, C.; Meng, Q.; Liu, C. The interface evolution during methane hydrate dissociation within quartz sands and its implications to the permeability prediction based on NMR data. *Mar. Pet. Geol.* **2021**, *129*, No. 105065.
(63) Peters, K. E. Guidelines for evaluating petroleum source rock using programmed pyrolysis. *AAPG Bull.* **1986**, *70*, 318−329.
(64) Peters, K. E.; Cassa, M. R. Applied source rock geochemistry. *AAPG Memoir* **1994**, *60*, 93.
(65) Sanei, H.; Petersen, H. I.; Schovsbo, N. H.; Jiang, C.; Goodsite, M. E. Petrographic and geochemical composition of kerogen in the Furongian (U. Cambrian) Alum Shale, Central Sweden: Reflections on the petroleum generation potential. *Int. J. Coal Geol.* **2014**, *132*, 158−169.
(66) Li, Y.; Wang, Z.; Gan, Q.; Niu, X.; Xu, W. Paleoenvironmental conditions and organic matter accumulation in Upper Paleozoic organic-rich rocks in the east margin of the Ordos Basin, China. *Fuel* **2019**, *252*, 172−187.
(67) Zhao, W.; Zhang, B.; Wang, X.; Wu, S.; Zhang, S.; Liu, W.; Wang, K.; Zhao, X. Differences in source kitchens for lacustrine in-source and out-of-source hydrocarbon accumulations. *Pet. Explor. Dev.* **2021**, *48*, 541−554.
(68) Gamero-Diaz, H.; Miller, C.; Lewis, R. SCore: A mineralogy based classification scheme for organic mudstones. *SPE Annu. Tech. Conf. Exhib.* **2013**, *3*, 2465−2481.
(69) Liang, M.; Wang, Z.; Gao, L.; Li, C.; Li, H. Evolution of pore structure in gas shale related to structural deformation. *Fuel* **2017**, *197*, 310−319.
(70) Chalmers, G. R.; Bustin, R. M.; Power, I. M. Characterization of gas shale pore systems by porosimetry, pycnometry,surface area, and field emission scanning electron microscopy/ transmission electron microscopy image analyses: Examples from the Barnett, Woodford, Haynesville, Marcellus, and Doig units. *AAPG Bull.* **2012**, *96*, 1099−1119.
(71) Chalmers, G. R. L.; Bustin, R. M. Lower cretaceous gas shales in northeastern British Columbia, Part I: geological controls on methane sorption capacity. *Bull. Can. Pet. Geol.* **2008**, *56*, 1−21.
(72) Wang, Y.; Liu, L.; Zheng, S.; Luo, Z.; Sheng, Y.; Wang, X. Full-scale pore structure and its controlling factors of the Wufeng-Longmaxi shale, southern Sichuan Basin, China: Implications for pore evolution of highly overmature marine shale. *J. Nat. Gas Sci. Eng.* **2019**, *67*, 134−146.
(73) Gou, Q.; Xu, S.; Hao, F.; Yang, F.; Zhang, B.; Shu, Z.; Zhang, A.; Wang, Y.; Lu, Y.; Cheng, X.; Qing, J.; Gao, M. Full-scale pores and micro-fractures characterization using FE-SEM, gas adsorption, nano-CT and micro-CT: A case study of the Silurian Longmaxi Formation shale in the Fuling Area, Sichuan Basin, China. *Fuel* **2019**, *253*, 167−179.
(74) Cao, Z.; Jiang, H.; Zeng, J.; Saibi, H.; Lu, T.; Xie, X.; Zhang, Y.; Zhou, G.; Wu, K.; Guo, J. Nanoscale liquid hydrocarbon adsorption on clay minerals: A molecular dynamics simulation of shale oils. *Chem. Eng. J.* **2021**, *420*, No. 127578.
(75) Pang, X.; Wang, G.; Kuang, L.; Li, H.; Zhao, Y.; Li, D.; Zhao, X.; Wu, S.; Feng, Z.; Lai, J. Insights into the pore structure and oil mobility in fine-grained sedimentary rocks: The Lucaogou Formation in Jimusar Sag, Junggar Basin, China. *Mar. Pet. Geol.* **2022**, *137*, No. 105492.
(76) Wu, T.; Pan, Z.; Liu, B.; Connell, L. D.; Sander, R.; Fu, X. Laboratory Characterization of shale oil storage behavior: A comprehensive review. *Energy Fuels* **2021**, *35*, 7305−7318.
(77) Xu, H.; Zhou, W.; Zhang, R.; Liu, S.; Zhou, Q. Characterizations of pore, mineral and petrographic properties of marine shale using multiple techniques and their implications on gas storage capability for Sichuan Longmaxi gas shale field in China. *Fuel* **2019**, *241*, 360−371.
(78) Ji, W.; Hao, F.; Song, Y.; Tian, J.; Meng, M.; Huang, H. Organic geochemical and mineralogical characterization of the lower Silurian Longmaxi shale in the southeastern Chongqing area of China: Implications for organic matter accumulation. *Int. J. Coal Geol.* **2020**, *220*, No. 103412.
(79) Zhang, S.; Liu, C.; Liang, H.; Wang, J.; Bai, J.; Yang, M.; Liu, G.; Huang, H.; Guan, Y. Paleoenvironmental conditions, organic matter accumulation, and unconventional hydrocarbon potential for the Permian Lucaogou Formation organic-rich rocks in Santanghu Basin, NW China. *Int. J. Coal Geol.* **2018**, *185*, 44−60.
(80) Peltonen, C.; Marcussen, Ø.; Bjørlykke, K.; Jahren, J. Clay mineral diagenesis and quartz cementation in mudstones: The effects of smectite to illite reaction on rock properties. *Mar. Pet. Geol.* **2009**, *26*, 887−898.
(81) Milliken, K. L.; Rudnicki, M.; Awwiller, D. N.; Zhang, T. Organic matter-hosted pore system, Marcellus Formation (Devonian), Pennsylvania. *AAPG Bull.* **2013**, *97*, 177−200.
(82) Wu, L.; Geng, A.; Wang, P. Oil expulsion in marine shale and its influence on the evolution of nanopores during semi-closed pyrolysis. *Int. J. Coal Geol.* **2018**, *191*, 125−134.
(83) Jarvie, D. M.; Hill, R. J.; Ruble, T. E.; Pollastro, R. M. Unconventional shale-gas systems: The Mississippian Barnett Shale of north-central Texas as one model for thermogenic shale-gas assessment. *AAPG Bull.* **2007**, *91*, 475−499.
(84) Jin, Z.; Liang, X.; Bai, Z. Exploration breakthrough and its significance of Gulong lacustrine shale oil in the Songliao Basin, northeastern China. *Energy Geosci.* **2022**, *3*, 120−125.
(85) Liu, D.; Li, Z.; Jiang, Z.; Zhang, C.; Zhang, Z.; Wang, J.; Yang, D.; Song, Y.; Luo, Q. Impact of laminae on pore structures of lacustrine shales in the southern Songliao Basin, NE China. *J. Asian Earth Sci.* **2019**, *182*, No. 103935.

NOTE ADDED AFTER ASAP PUBLICATION

This paper was published on July 22, 2022, with a highlights section, which is not published in this journal. This section was deleted in the version published on July 25, 2022.

https://doi.org/10.1021/acs.energyfuels.2c01484
Energy Fuels 2022, 36, 8161−8179